

REPORT DOCUMENTATION PAGE

Form Approved OMB No. 0704-0188

Public reporting burden for this collection of information is estimated to average 1 hour per response, including the time for reviewing instructions, searching existing data sources, gathering and maintaining the data needed, and completing and reviewing the collection of information. Send comments regarding this burden estimate or any other aspect of this collection of information, including suggestions for reducing the burden, to Department of Defense, Washington Headquarters Services, Directorate for Information Operations and Reports (0704-0188), 1215 Jefferson Davis Highway, Suite 1204, Arlington, VA 22202-4302. Respondents should be aware that notwithstanding any other provision of law, no person shall be subject to any penalty for failing to comply with a collection of information if it does not display a currently valid OMB control number.
PLEASE DO NOT RETURN YOUR FORM TO THE ABOVE ADDRESS.

1. REPORT DATE (DD-MM-YYYY) 05-02-2010	2. REPORT TYPE Final Report	3. DATES COVERED (From – To) 01-Dec-06 - 11-Jun-10
--	---------------------------------------	--

4. TITLE AND SUBTITLE Development of high strength thermally stable Al-based alloys with nanocomposite structure	5a. CONTRACT NUMBER STCU Registration No: P-280
	5b. GRANT NUMBER
	5c. PROGRAM ELEMENT NUMBER

6. AUTHOR(S) Professor Valeriy Victorovich Maslov	5d. PROJECT NUMBER
	5d. TASK NUMBER
	5e. WORK UNIT NUMBER

7. PERFORMING ORGANIZATION NAME(S) AND ADDRESS(ES) Institute for Metal Physics, NAS of Ukraine 36 Vernadsky str. Kiev 03142 Ukraine	8. PERFORMING ORGANIZATION REPORT NUMBER N/A
--	--

9. SPONSORING/MONITORING AGENCY NAME(S) AND ADDRESS(ES) EOARD Unit 4515 BOX 14 APO AE 09421	10. SPONSOR/MONITOR'S ACRONYM(S)
	11. SPONSOR/MONITOR'S REPORT NUMBER(S) STCU 06-8005

12. DISTRIBUTION/AVAILABILITY STATEMENT

Approved for public release; distribution is unlimited.

13. SUPPLEMENTARY NOTES

14. ABSTRACT

This report results from a contract tasking Institute for Metal Physics, NAS of Ukraine as follows: The demands on materials set by aerospace and aircraft manufacturers include the development of alloys possessing high strength-to-weight ratios and capable to withstand high temperature exposures during service. One of the promising classes of materials which may meet these requirements are Al-based alloys with nanocomposite structures formed by partial crystallization of amorphous precursors the strength of which may exceed 1500 MPa. Solution of the problems concerning alloys chemistry and ability to tailor of certain microstructures is of prime importance for the development of new nanostructured materials.

The goals of the project are to perform the systematic experimental studies of the effects of alloy composition and thermal prehistory on glass-forming ability, thermal stability, crystallization behaviour and mechanical properties of a series binary, ternary and multicomponent Al-based alloys alloyed by transition metals and rare earths as well as to elaborate appropriate theoretical models of nanocrystallization processes. The main factors responsible for nanoscale microstructure formation will be determined from comparison of the experimental data with the model predictions.

As a result a series of new Al-based alloys with nanocomposite structure with improved mechanical properties and enhanced thermal stability will be developed and the fundamental basis for the nanostructured alloys design will be created.

15. SUBJECT TERMS
EOARD, Materials, Metallurgy and Metallography

16. SECURITY CLASSIFICATION OF:			17. LIMITATION OF ABSTRACT UL	18. NUMBER OF PAGES 26	19a. NAME OF RESPONSIBLE PERSON WYNN SANDERS, Maj, USAF
a. REPORT UNCLAS	b. ABSTRACT UNCLAS	c. THIS PAGE UNCLAS			19b. TELEPHONE NUMBER (Include area code) +44 (0)1895 616 007

Development of new high strength bulk structural aluminum alloys with nanocomposite structure

Project manager: Valeriy V. Maslov, Prof., Dr. of Phys.-Math.Sci., Head of crystallization department
 Phone: +380 (44) 424-3241; fax: +380 (44) 424-3505; E-mail: maslov@imp.kiev.ua
 Institutions: : G.V.Kurdyumov Institute of Metal Physics of NAS of Ukraine
 Financing parties: USA (EOARD)
 Operative commencement date: 01.12.2006
 Project duration: 01 December 2006 – 30 November 2009
 Date of submission: 17.02.2009

Content of final annual report

1	Summary	3
2	Introduction	3
3	Methods, Assumptions, and Procedures	4
4	Results and Discussion	6
	Activity 2. Studies of thermal stability of the amorphous phases and crystallization behaviour during heat treatment of the Al-based alloys with various chemical composition	6
	Activity 2.1. Experimental studies of kinetics and mechanisms of nanocrystallization of amorphous Al-based alloys	6
	Activity 2.2. Determination of the parameters of nanocomposite structures as a function of alloy chemical composition and thermal prehistory of the amorphous Al-based alloys	10
	Activity 2.3. Studies of the temperature/time limits of stability of nanocomposite structure in the Al-based alloys	15
	Activity 2.4. Development of theoretical models of nanocrystallization at isothermal conditions as upon constant rate heating and comparison with the experimental data; quantitative estimations of the parameters governing thermal stability of amorphous phases with various chemical composition, the sizes and volume density of nanocrystals and glass forming ability of the melts	17
	Activity 2.5. Studies of thermal stability of the amorphous phases and crystallization behaviour during heat treatment of the Al-based alloys with various chemical composition	19
5	Conclusions	22
6	References	23
7	List of Symbols, Abbreviations, and Acronyms	25

List of Figures

Fig.1	Changes of normalized resistance (left axis) and the derivative of dR/dT (right axis) during heating of amorphous $Al_{90}Y_{10}$ melt spun ribbon recorded at heating rate of 5 K/min, where R_0 is the electrical resistance at room temperature. The arrow shows the onset crystallization temperature.	5
Fig.2	X-ray diffraction patterns of the $Al_{90}Y_{10}$ melt-spun ribbons heated up to temperatures corresponding to those (a) of the end of the first stage crystallization (502 K) and (b) to the completion of crystallization (564 K).	5

- Fig. 3 Changes of normalized electrical resistance during heating of the amorphous melt spun ribbons recorded at heating rate of 5 K/min: (a) $\text{Al}_{90}\text{Y}_{10}$ (Δ), $\text{Al}_{90}\text{Gd}_{10}$ (\circ), $\text{Al}_{87}\text{Ni}_8\text{Y}_5$ (\blacktriangle), $\text{Al}_{87}\text{Ni}_8\text{Gd}_5$ (\bullet); b) $\text{Al}_{87}\text{Ni}_8\text{Gd}_5$ (\circ), $\text{Al}_{87}\text{Ni}_8\text{Gd}_1\text{Y}_4$ (\bullet), $\text{Al}_{87}\text{Ni}_4\text{Fe}_4\text{Gd}_5$ (Δ), $\text{Al}_{87}\text{Ni}_4\text{Fe}_4\text{Gd}_1\text{Y}_4$ (\blacktriangle); c) $\text{Al}_{86}\text{Ni}_6\text{Co}_2\text{Gd}_6$ (\circ), $\text{Al}_{86}\text{Ni}_2\text{Co}_6\text{Gd}_6$ (Δ), $\text{Al}_{86}\text{Ni}_6\text{Fe}_2\text{Gd}_6$ (\bullet), $\text{Al}_{86}\text{Ni}_2\text{Fe}_6\text{Gd}_6$ (\blacktriangle). 7
- Fig. 4 Fig. 4. Kissinger plots derived from the crystallization peak temperatures, T_{x1} , for the amorphous alloys: (a) $\text{Al}_{90}\text{Y}_{10}$ (Δ), $\text{Al}_{90}\text{Gd}_{10}$ (\circ), $\text{Al}_{87}\text{Ni}_8\text{Y}_5$ (\blacktriangle), $\text{Al}_{87}\text{Ni}_8\text{Gd}_5$ (\bullet); b) $\text{Al}_{87}\text{Ni}_8\text{Gd}_5$ (\circ), $\text{Al}_{87}\text{Ni}_8\text{Gd}_1\text{Y}_4$ (\bullet), $\text{Al}_{87}\text{Ni}_4\text{Fe}_4\text{Gd}_5$ (Δ), $\text{Al}_{87}\text{Ni}_4\text{Fe}_4\text{Gd}_1\text{Y}_4$ (\blacktriangle); c) $\text{Al}_{86}\text{Ni}_6\text{Co}_2\text{Gd}_6$ (\circ), $\text{Al}_{86}\text{Ni}_2\text{Co}_6\text{Gd}_6$ (Δ), $\text{Al}_{86}\text{Ni}_6\text{Fe}_2\text{Gd}_6$ (\bullet), $\text{Al}_{86}\text{Ni}_2\text{Fe}_6\text{Gd}_6$ (\blacktriangle). 8
- Fig. 5 X-ray diffraction patterns of the as prepared (curves 1) melt-spun ribbons and heated up at 5 K/min to the end temperatures of first (curves 2), second (curves 4) and third (curves 4) crystallization stages indicated in the plots: (a) - $\text{Al}_{86}\text{Ni}_6\text{Co}_2\text{Gd}_6$; (b) - $\text{Al}_{87}\text{Ni}_8\text{Gd}_5$; (c) $\text{Al}_{86}\text{Ni}_2\text{Fe}_6\text{Gd}_6$. 10
- Fig. 6 X-ray diffraction patterns of the samples heated up at 5 K/min to temperatures of the first crystallization stage end: 1 - $\text{Al}_{87}\text{Ni}_4\text{Fe}_4\text{Gd}_5$, 2 - $\text{Al}_{87}\text{Ni}_4\text{Fe}_4\text{Gd}_1\text{Y}_4$. 11
- Fig. 7 X-ray diffraction patterns of the samples heated up at 5 K/min to temperatures of the first crystallization stage end: 1 - $\text{Al}_{86}\text{Ni}_2\text{Co}_6\text{Gd}_6$, 2 - $\text{Al}_{86}\text{Ni}_2\text{Fe}_6\text{Gd}_6$. 11
- Fig. 8 Effect of partial replacement of Ni with Co on the rate of the first stage of crystallization of the Al-based amorphous alloys at 5 K/min: 1 - $\text{Al}_{86}\text{Ni}_6\text{Co}_2\text{Gd}_6$; 2 - $\text{Al}_{86}\text{Ni}_4\text{Co}_4\text{Gd}_6$; 3 - $\text{Al}_{86}\text{Ni}_2\text{Co}_6\text{Gd}_6$. 11
- Fig. 9 Effect of partial replacement of Ni with Fe on the rate of the first stage of crystallization of the Al-based amorphous alloys at 5 K/min: 1 - $\text{Al}_{87}\text{Ni}_8\text{Gd}_5$; 2 - $\text{Al}_{87}\text{Ni}_4\text{Fe}_4\text{Gd}_5$; 3 - $\text{Al}_{86}\text{Ni}_2\text{Fe}_6\text{Gd}_6$. 11
- Fig. 10 Isothermal kinetic curves of the first crystallization stage (nanocrystallization) of the amorphous alloys derived from the resistometric data normalized to the volume fraction crystallized determined from the XRD data: a) $\text{Al}_{90}\text{Y}_{10}$, b) $\text{Al}_{86}\text{Ni}_6\text{Co}_2\text{Gd}_6$ and c) $\text{Al}_{86}\text{Ni}_2\text{Co}_6\text{Gd}_6$. 12
- Fig. 11 Avrami plots for amorphous $\text{Al}_{90}\text{Y}_{10}$ alloy from the data presented in Fig. 10(a) for annealing temperatures 447 K (a) and 460 K (b). 13
- Fig. 12 Avrami plots for amorphous $\text{Al}_{86}\text{Ni}_6\text{Co}_2\text{Gd}_6$ alloy from the data presented in Fig. 6 (b) for annealing temperatures 461 K (a) and 501 K (b). 14
- Fig. 13 Avrami plots for amorphous $\text{Al}_{86}\text{Ni}_2\text{Co}_6\text{Gd}_6$ alloy from the data presented in Fig. 6(c) for annealing temperatures 525 K (a) and 560 K (b). 14
- Fig. 14 Effect of crystallization on microhardness (right axis) of amorphous $\text{Al}_{90}\text{Y}_{10}$ (a) and $\text{Al}_{90}\text{Gd}_{10}$ (b) alloys. 16
- Fig. 15 Kissinger plots derived from crystallization peak temperatures, T_{X2} , for the amorphous alloys: (a) 1 - $\text{Al}_{86}\text{Ni}_2\text{Co}_6\text{Gd}_6$ (circles), 2 - $\text{Al}_{86}\text{Ni}_4\text{Co}_4\text{Gd}_2\text{Y}_4$ (triangles), 3 - $\text{Al}_{86}\text{Ni}_6\text{Co}_2\text{Gd}_6$ (squares); (b) 1 - $\text{Al}_{86}\text{Ni}_2\text{Fe}_6\text{Gd}_6$ (triangles), 2 - $\text{Al}_{87}\text{Ni}_4\text{Fe}_4\text{Gd}_5$ (squares), 3 - $\text{Al}_{87}\text{Ni}_8\text{Gd}_5$ (circles). 17
- Fig. 16 Changes of the relative electrical resistance (left axis) and the volume fraction transformed (right axis) under isothermal annealing of amorphous alloys (a) $\text{Al}_{90}\text{Y}_{10}$ at 487 K and (b) $\text{Al}_{86}\text{Ni}_6\text{Co}_2\text{Gd}_6$ at 575 K. 18
- Fig. 17 Avrami plots for isothermal two stage crystallization of (a) $\text{Al}_{90}\text{Y}_{10}$ at 487 K and (b) $\text{Al}_{86}\text{Ni}_6\text{Co}_2\text{Gd}_6$ at 575 K from the data presented in Fig. 16. 19
- Fig. 18 The schematic representation of the "soft impingement" of growing primary nanocrystals. The symbols on the graph are described in text. 20
- Fig. 19 Changes of the average grain size of Al-nanocrystals in amorphous $\text{Al}_{90}\text{Y}_{10}$ alloy at isothermal annealing at 447 K (\bullet), 458 K (\blacktriangle) and 487 K (\square). The dashed curves were fitted by Eq. (5). 21

Fig. 20	Changes of the average grain size of Al-nanocrystals in amorphous $\text{Al}_{86}\text{Ni}_6\text{Co}_2\text{Gd}_6$ alloy at isothermal annealing at 443 (●) and 473 K (■). The dashed curves were fitted by Eq. (5).	21
Fig. 21	Comparison of the temperature dependencies of the effective diffusion coefficients which govern Al-nanocrystals growth in amorphous $\text{Al}_{90}\text{Y}_{10}$ (■) and $\text{Al}_{86}\text{Ni}_6\text{Co}_2\text{Gd}_6$ (▲) extracted from the data shown in Fig. with the self diffusion coefficient of fcc Al [41] (solid lines). The dashed lines are linear approximation of the estimated data.	21
List of Tables		
Table 1	Chemical composition, average ribbon thickness and the parameters of thermal stability of the amorphous alloys	7
Table 2	Chemical composition, structure of the alloys after the first crystallization stage, activation energies, microhardness of the nanophase composites and increment of microhardness after the first crystallization stage	9
Table 3	Chemical composition, structural parameters of nanophase composites, microhardness and its increment after the first crystallization stage of continuously heated samples.	15
Table 4	Comparison of the parameters of nanocomposite structures obtained at isothermal conditions and at continuous heating	15
Table 5	Chemical composition, number of casting run and the parameters of thermal stability of amorphous and nanocomposite alloys	17

1. Summary

Studies have been carried out according to the approved technical schedule (Task 2) and the personal executors plans for the second year. At the substage 2.1 experiments on continuous heating of the 12 binary, ternary, quaternary and quinary amorphous $\text{Al}_{90-86}(\text{Ni}, \text{Co}, \text{Fe})_{6-8}(\text{Y}, \text{Gd}, \text{Tb})_{6-10}$ alloys have been performed and it has been established that crystallization begins at temperatures 440–584 K by formation of the nanocomposite structures (nanocrystals embedded in the residual amorphous matrix) and occurs in the 2 or 3 well-defined stages. The three different nanocrystallization mechanisms of the first crystallization stage have been established including: (1) diffusion limited growth of the quenched-in Al nuclei, (2) nucleation and subsequent diffusion limited growth of Al nanocrystals and (3) nucleation and simultaneous growth of nanoscale crystals of Al and intermetallic compounds (substage 2.1). It has been established (substage 2.3) that formation of nanophase composites having the crystallized volume fractions, the average sizes of Al nanocrystals and the densities in the ranges (0.22–0.59), (14.8–21.0) nm and $(1.1–4.3) \times 10^{23} \text{ m}^{-3}$, respectively, results in essential increasing of the microhardness (by 740–1740 MPa) in comparison with that of amorphous phases. The nanophase composites are stable in the experimentally measured temperature ranges of 12–143 K with upper temperature limits of 520–619 K (substage 2.4) where crystallization of the intermetallic phases occurs. The analytical model assuming retardation of the diffusion-limited growth due to impingement of the diffusion fields has been applied for description the experimental data and the effective diffusion coefficients governing the growth of nanocrystals in amorphous $\text{Al}_{86}\text{Ni}_6\text{Co}_2\text{Gd}_6$ and $\text{Al}_{90}\text{Y}_{10}$ alloys have been estimated (substage 2.5). There was no scheduling variance in the reporting period.

2. Introduction

Technical progress requires strong and light materials. Al-based amorphous alloys, containing 8–20 at.% rare earths (RE) and transition metals (TM) possess high tensile strength [1,2] as well as high specific strength due to low density of Al and hence attracted increasing interest for a large number of technical applications as light and high-strength structural materials, for example for aerospace applications and so on. Moreover, it has been shown [2–4] that the mechanical properties of amorphous alloys can be essentially improved (about 1.5 times) by partial crystallization, which results in formation of Al particle diameters in the range 3–50 nm, particle separation 10–100 nm, and the α -Al volume fraction 10–30%. However, until now, these properties were obtained in thin ribbons produced by the melt-spinning technique so the application of such nanophase composites as structural materials is restricted. To obtain bulk Al-based materials with nanocomposite

structure, two basic strategies may be used – search the alloy compositions with high glass forming ability [5] and consolidation of melt-spun ribbons or powders with amorphous structure [6,7].

Since the key process which determines the nanocrystal size and their volume density as well the thermomechanical regimes of consolidation required to keep nanocomposite structure is nanocrystallization the studies of this project stage have been focused on establishment of the mechanisms this process. The activity includes the experimental investigations of thermal stability of amorphous phases in a number of Al-(Ni,Co,Fe)-(Y,Gd) melt-spun ribbons, the estimations of the structural parameters of nanophase composites, the establishment of nanocrystallization mechanisms and the development of the relevant theoretical models of the process of formation nanophase composites.

The main goals of these studies are to obtain information concerning the effect of alloying on thermal stability of amorphous alloys and nanophase composites, on crystallization mechanisms and on the structural parameters of partially crystallized alloys as well as to develop the technique for estimation of the main factors responsible for nanoscale microstructure formation. The obtained results have to provide basis for selection of the alloys with improved both thermal stability and microhardness for subsequent advanced investigations and optimization of their mechanical properties.

3. Methods, Assumptions, and Procedures

In order to estimate of the influence of alloying on glass forming ability of Al-based melts as well as on thermal stability, structure, microhardness, mechanisms of nanocrystallization of amorphous phases a series of 12 binary, ternary, quaternary and quinary $\text{Al}_{90-86}(\text{Ni,Co,Fe})_{6-8}(\text{Y,Gd,Tb})_{6-10}$ alloys has been prepared by arc melting under highly purified argon atmosphere and rapidly quenched from liquid state by the melt-spinning processing under a helium atmosphere.

Glass forming ability of the alloys has been qualitative estimated at this stage from the specific features of the X-ray diffraction patterns. Thermal stability of both amorphous phases and partially crystallized nanocomposite structures has been studied by monitoring of electrical resistance changes under continuous constant rate heating.

The structural parameters of nanophase composites (average size of nanocrystals, their volume density and the volume fraction) have been estimated from X-ray diffraction data.

For estimation of crystallization mechanisms the isothermal kinetic crystallization curves obtained by combination of electrical resistance measurements and X-ray analysis data have been used.

The relatively simple analytical model, describing changes of sizes of Al nanocrystals versus time at constant temperature, has been proposed and the values of the effective diffusion coefficient, which governs the growth of nanocrystals, have been estimated from comparison between the calculated and experimental data.

The effect of nanocrystallization on mechanical properties has been estimated from the microhardness measurements.

Amorphous $\text{Al}_{90-86}(\text{Ni,Co,Fe})_{6-8}(\text{Y,Gd,Tb})_{6-10}$ alloys have been obtained by single roller melt spinning technique in the form of ribbons 5–10 mm wide and 35–90 μm thick as described in the previous annual report.

The electrical resistance of ribbons has been measured *in situ* by the automated four-probe dc method in which thermal emf effects were accounted by averaging for positive and negative voltages. Electrical contacts to the samples of as-cast and heat-treated ribbons were made by spot-welding of silver wires about 50 μm in diameter.

The constant heating experiments were performed at scan rates ranging from 5 to 40 K/min using a standard PRT-1000 device. The measurements of the electrical resistance at continuous heating has shown that it drops at several (from 2 to 2) stages as illustrated in Fig.1 for amorphous $\text{Al}_{90}\text{Y}_{10}$ alloy. The X-ray diffraction patterns of the samples heated to the temperatures above each stage which are clearly resolved in dR/dT curves has shown that each stage results in structural changes (Fig. 2). It indicates that crystallization of the amorphous $\text{Al}_{90}\text{Y}_{10}$ alloy is multi-stage process which is typical for Al-based glasses [8,9]. It should be noted that as it has been shown in [8] the resistometry scan of the $\text{Al}_{85}\text{Ni}_5\text{Y}_8\text{Co}_2$ glass not only well agrees with the DSC thermogram, but is more sensitive for the detection of the phase transformations. Therefore, the characteristic temperatures of amorphous \rightarrow crystalline transformation (onset crystallization, T_{ons} , and maximum rate of crystallization, T_{x}) in the present study have been determined from the resistometric data as shown in Fig. 1.

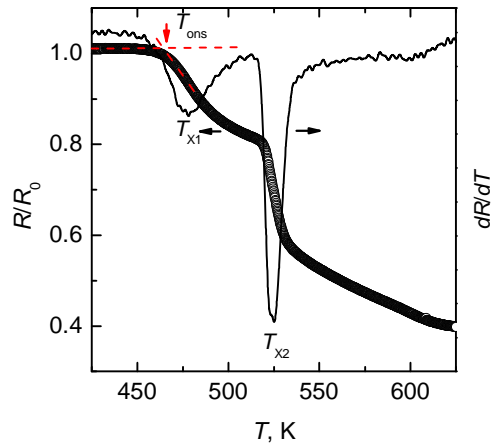


Fig. 1. Changes of normalized resistance (left axis) and the derivative of dR/dT (right axis) during heating of amorphous $\text{Al}_{90}\text{Y}_{10}$ melt spun ribbon recorded at heating rate of 5 K/min, where R_0 is the electrical resistance at room temperature. The arrow shows the onset crystallization temperature.

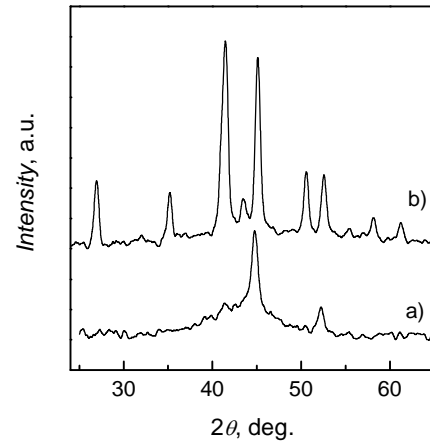


Fig. 2. X-ray diffraction patterns of the $\text{Al}_{90}\text{Y}_{10}$ melt-spun ribbons heated up to temperatures corresponding to those (a) of the end of the first stage crystallization (502 K) and (b) to the completion of crystallization (564 K).

Isothermal anneals were carried out by immersing small pieces of melt-spun ribbons in silicone oil (below 573 K) or salt (eutectic mixture of NaNO_3 , KNO_3 and LiNO_3) bathes with temperature controlled to ± 1.0 K. The measured heat-up times in the liquid bathes were typically from 3 to 4 s.

The structural characterization of the partially crystallized ribbons was carried out by X-ray diffraction using Fe-filtered $\text{CoK}\alpha$ radiation ($\lambda = 0.1791$ nm) in a standard DRON-3M diffractometer. The amorphous and nanocrystalline total intensity contributions, shown in Fig. 2 (a) were obtained by deconvolution [10] of the first amorphous halo and the two most intense ((111) and (200)) fcc-Al peaks after background subtraction. The Lorentzian function fits were chosen for matching both amorphous halo and broadened fcc-Al peaks according to the best agreement with experimental data.

The special attention in this part of studies was paid to determination of the volume fraction of Al nanocrystals, X , in the partially crystallized samples with nanocomposite structure, because there is no well established technique of evaluation of this quantity. The comparative analysis presented in Ref. [11] has shown that the widely used relation [12]

$$X = A_c / (A_a + A_c) \quad (1)$$

(where A_c and A_a being the sum of the areas of the (111) and (200) reflections of Al and that of amorphous halo, respectively) underestimates the volume fraction of Al nanocrystals in a residual amorphous matrix. The physical reason of this is an enhanced average scattering power of the amorphous phase in comparison with that of pure Al. It has been proposed to use multiplying the value of A_a by a correction factor (less than unity) [13] or the Rietveld procedure [11] to account the discrepancy in estimations of X . The more direct approach to account the difference between the between the scattering power of amorphous and nanocrystalline phases of different chemical compositions was proposed in Ref. [14]

$$\frac{A_c}{A_c + A_a} = \frac{X \langle f \rangle_c^2}{X \langle f \rangle_c^2 + (1 - X) \langle f \rangle_a^2}, \quad (2)$$

where $\langle f \rangle$ is the average scattering factors of amorphous matrix and nanocrystalline phase. The above mentioned approaches for estimation of X were used to determine the volume fraction of Al nanocrystals in the samples of the binary amorphous $\text{Al}_{90}\text{Y}_{10}$ alloy heated up to the temperatures corresponding the end of the first and second crystallization stages (Fig. 1).

The values of X in the sample after the first crystallization stage calculated from Equations (1) and (2) were 29 and 45%, respectively. In view, that the dominating process of the second crystallization stage is formation of the Al_3Y intermetallic compound which volume fraction in the fully crystallized sample according the level rule is 40 %, the volume fraction of Al nanocrystals after nanocrystallization calculated from Eq. (2) seems rather reasonable. It should be also noted that the calculated difference between X calculated from Eq. (1) and

(2) is close to that obtained from Eq. (1) and from Rietveld method for $\text{Al}_{87}\text{Ni}_7\text{La}_5\text{Zr}_1$ [11] and corresponds the value of 0.5 for the correction factor proposed in Ref. [13].

The microhardness (H_μ) measurements of the heat treated melt-spun ribbons were performed using standard PMT-3 microhardness tester calibrated with a NaCl monocrystal. The measurements were carried out on the flat areas presumably contact surfaces of 15 specimens at a load of 0.29 N (30 gf) during 10 s. The H_μ values for each specimen were determined by averaging of 10 indents with regular shape which gave the standard deviation of the data about $\pm 1.5\%$.

4. Results and Discussion

Activity 2. Clarification of regularities of the Al-nanocomposite formation processes

As it has been mentioned above, the nanocomposite structures formed in partially crystallized Al-based alloys are the most important from practical point of view. Therefore, at this project stage the nanocrystallization process is the main focus of the studies aimed to clarify it. These studies include the experimental determination of thermal stability of both amorphous and partially crystallized structures, estimation of the structural parameters of nanophase composites, kinetics and mechanisms of nanocrystallization and development of relevant theoretical models describing formation of nanocrystals in amorphous phases. The results of these studies will provide the basis for quantitative analysis of the process of formation nanophase composites.

Activity 2.1. Studies of thermal stability of the amorphous phases and crystallization behaviour during heat treatment of the Al-based alloys with various chemical composition

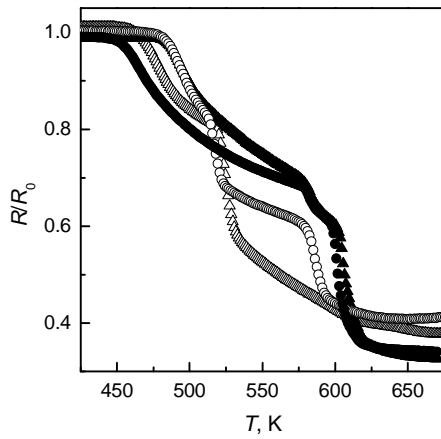
Thermal stability of amorphous state is a very important property of amorphous alloys which marks limiting temperatures (at continuous heating) or times (at isothermal conditions) of their existence. In the present study the crystallization onset temperature, T_{ons} , determined at heating rate of 5 K/min (Fig. 1) has been taken as a measure of kinetic thermal stability of glassy alloys with various chemical composition. For this purpose the measurements of the electrical resistance of the melt-spun ribbons have been carried out and the obtained curves are shown in Fig. 3.

As can be seen in this Figure both the thermal stability and crystallization behavior of the amorphous Al-based alloys depend on their chemical composition, however, the alloying effects are ambiguous. In fact, the full and even partial replacement of Y by Gd in $\text{Al}_{87}\text{Ni}_8\text{Gd}_5$ alloy results in essential lowering of thermal stability (Fig 3a,b), in contrast to higher T_{ons} of binary $\text{Al}_{90}\text{Gd}_{10}$ alloy in comparison with that of $\text{Al}_{90}\text{Y}_{10}$ (Fig. 3a). At the same time the variations of content of transition metals have an evident effect on thermal stability of amorphous phases, namely partial substitution of Ni for Co and especially Fe increases T_{ons} (Fig. 3b,c). Note, that the positive effect of Ni replacement with Co or Fe on thermal stability amorphous Al-(Ni,Co,Fe)-RE alloys has been recently reported in literature [15-17]. Besides, the change of Ni/(Co,Fe) proportions from 3/1 to 1/3 leads to lowering of the number of crystallization stages from 3 (which is typical for the majority amorphous alloys studied) to 2 (Fig. 3c).

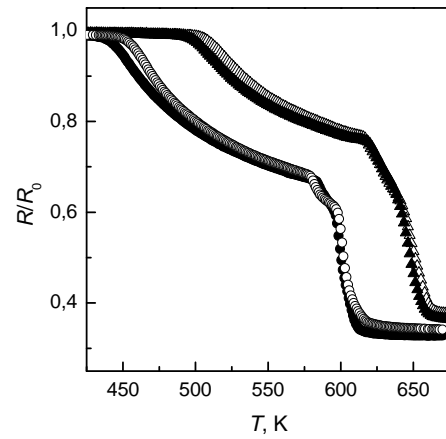
The values of the onset crystallization temperatures summarized in Table 1 range from 440 ($\text{Al}_{87}\text{Ni}_4\text{Fe}_4\text{Gd}_1\text{Y}_4$) to 584 K ($\text{Al}_{86}\text{Ni}_2\text{Fe}_6\text{Gd}_6$) and are rather high in comparison with those reported in literature for Al-based amorphous alloys (e.g., [15-18]).

The continuous heating experiments at rates of 5, 10, 20 and 40 K/min were used to determine the activation energy of the first crystallization stage, Q_1 , which is a useful parameter of the crystallization process. For this purpose the well-known method proposed by Kissinger [19] was used. In the standard Kissinger analysis of a nucleation-and-growth process the activation energy is determined by plotting, for a number of scans at different rates, q , $\ln(T_X^2/q)$ vs. $(1/T_X)$, where T_X is the peak temperature (maximum rate) of transformation determined as shown in Fig. 1. The slope of a straight line fit through the plot is then Q/k_B (k_B being the Boltzmann constant).

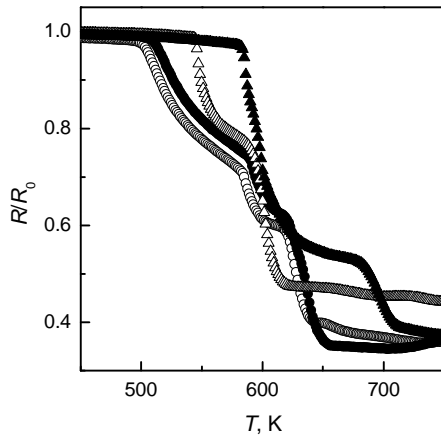
The results of these experiments presented in Fig. 4 show that the crystallization temperatures T_{X1} in the Kissinger coordinates are close to the straight lines which indicates the correctness of the analysis. Such determined activation energies of the first crystallization stage of the amorphous alloys investigate are in the wide range from 17000 to 65800 K (1.47 – 5.7 eV) (Table 2). All these values agree with those estimated for



a)



b)



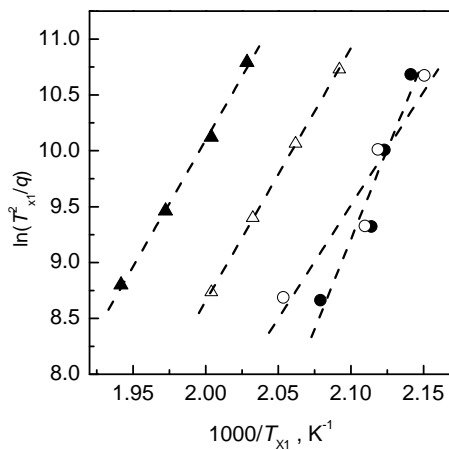
c)

Fig. 3. Changes of normalized electrical resistance during heating of the amorphous melt spun ribbons recorded at heating rate of 5 K/min: (a) $\text{Al}_{90}\text{Y}_{10}$ (Δ), $\text{Al}_{90}\text{Gd}_{10}$ (\circ), $\text{Al}_{87}\text{Ni}_8\text{Y}_5$ (\blacktriangle), $\text{Al}_{87}\text{Ni}_8\text{Gd}_5$ (\bullet); b) $\text{Al}_{87}\text{Ni}_8\text{Gd}_5$ (\circ), $\text{Al}_{87}\text{Ni}_8\text{Gd}_1\text{Y}_4$ (\bullet), $\text{Al}_{87}\text{Ni}_4\text{Fe}_4\text{Gd}_5$ (Δ), $\text{Al}_{87}\text{Ni}_4\text{Fe}_4\text{Gd}_1\text{Y}_4$ (\blacktriangle); c) $\text{Al}_{86}\text{Ni}_6\text{Co}_2\text{Gd}_6$ (\circ), $\text{Al}_{86}\text{Ni}_2\text{Co}_6\text{Gd}_6$ (Δ), $\text{Al}_{86}\text{Ni}_6\text{Fe}_2\text{Gd}_6$ (\bullet), $\text{Al}_{86}\text{Ni}_2\text{Fe}_6\text{Gd}_6$ (\blacktriangle).

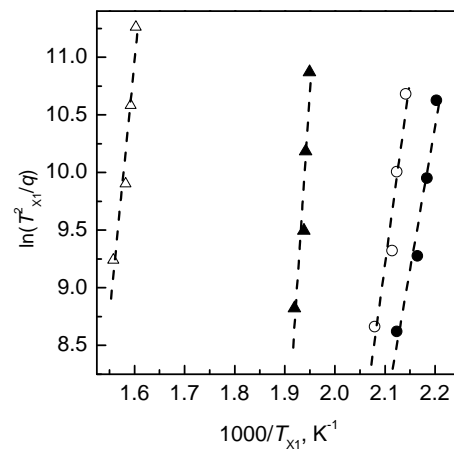
Table 1. Chemical composition, average ribbon thickness, number of crystallization stages and thermal stability of the amorphous alloys

	Alloy composition	No of casting run	Thickness, μm	Number of stages	T_{ons1} , K
1	$\text{Al}_{90}\text{Y}_{10}$	B-275	38 ± 6	2	464 ± 1
2	$\text{Al}_{90}\text{Gd}_{10}$	B-272	27 ± 2	3	476 ± 1
3	$\text{Al}_{87}\text{Ni}_8\text{Y}_5$	B-112	52 ± 5	3	484 ± 1
4	$\text{Al}_{87}\text{Ni}_8\text{Gd}_5$	B-252	35 ± 3	3	453 ± 1
5	$\text{Al}_{87}\text{Ni}_8\text{Gd}_1\text{Y}_4$	B-254	45 ± 5	3	440 ± 1
6	$\text{Al}_{86}\text{Ni}_6\text{Co}_2\text{Gd}_6$	B-276	50 ± 10	3	501 ± 1
7	$\text{Al}_{86}\text{Ni}_2\text{Co}_6\text{Gd}_6$	B-277	45 ± 6	2	545 ± 1
8	$\text{Al}_{86}\text{Ni}_6\text{Co}_2\text{Gd}_3\text{Y}_2\text{Tb}_1$	B-173	48 ± 10	3	500 ± 1
9	$\text{Al}_{87}\text{Ni}_4\text{Fe}_4\text{Gd}_5$	B-251	53 ± 8	3	506 ± 1
10	$\text{Al}_{87}\text{Ni}_4\text{Fe}_4\text{Gd}_1\text{Y}_4$	B-257	47 ± 2	3	497 ± 1
11	$\text{Al}_{86}\text{Ni}_6\text{Fe}_2\text{Gd}_6$	B-287	47 ± 3	3	509 ± 1
12	$\text{Al}_{86}\text{Ni}_2\text{Fe}_6\text{Gd}_6$	B-289	41 ± 3	2	584 ± 1

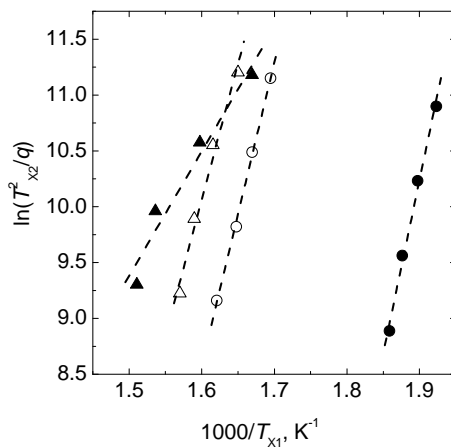
Al-based amorphous alloys (e.g. [15-18]) and are higher (except $\text{Al}_{90}\text{Gd}_{10}$) than Q of self-diffusion in pure Al (17130 K) [19] which indicates that the first crystallization stage of Al-based amorphous alloys is governed by diffusion of the solute atoms (transition and rare earth metals). In view, that due to technological difficulties the structure of the $\text{Al}_{90}\text{Gd}_{10}$ as prepared melt-spun ribbon was partially crystallized (Rep Qtr1_5) the value of Q_1 for this alloy may be underestimated. For this reason this amorphous alloy has been excluded from subsequent analysis. It should be noted that in contrast to the data of Ref. [15-17], there are no direct correlation between thermal stability of the amorphous phases and the activation energies of the first crystallization stage (Table 2). The possible reason for this is differences in the mechanisms of the first crystallization stage in Al-based amorphous alloys with different chemical compositions and this problem has been considered below.



a)



b)



c)

Fig. 4. Kissinger plots derived from the crystallization peak temperatures, T_{x1} , for the amorphous alloys: (a) $\text{Al}_{90}\text{Y}_{10}$ (Δ), $\text{Al}_{90}\text{Gd}_{10}$ (\circ), $\text{Al}_{87}\text{Ni}_8\text{Y}_5$ (\blacktriangle), $\text{Al}_{87}\text{Ni}_8\text{Gd}_5$ (\bullet); b) $\text{Al}_{87}\text{Ni}_8\text{Gd}_5$ (\circ), $\text{Al}_{87}\text{Ni}_8\text{Gd}_1\text{Y}_4$ (\bullet), $\text{Al}_{87}\text{Ni}_4\text{Fe}_4\text{Gd}_5$ (Δ), $\text{Al}_{87}\text{Ni}_4\text{Fe}_4\text{Gd}_1\text{Y}_4$ (\blacktriangle); c) $\text{Al}_{86}\text{Ni}_6\text{Co}_2\text{Gd}_6$ (\circ), $\text{Al}_{86}\text{Ni}_2\text{Co}_6\text{Gd}_6$ (Δ), $\text{Al}_{86}\text{Ni}_6\text{Fe}_2\text{Gd}_6$ (\bullet), $\text{Al}_{86}\text{Ni}_2\text{Fe}_6\text{Gd}_6$ (\blacktriangle).

In order to clarify the nature the processes which occur during transition of amorphous phases into crystalline state the X-ray diffraction studies of the samples heated up to the end temperatures of each crystallization stage have been performed. The analysis of the X-ray diffraction patterns has shown that crystallization The majority of the ternary and quaternary amorphous alloys investigated crystallize in three stage with Al nanocrystals formation in the first stage (Fig. 5a,b). However, the character of the phases formed in the second and third stages are different and less clear. As it can be seen in Fig. 5a after the second crystallization stage structure of partially crystallized $\text{Al}_{86}\text{Ni}_6\text{Co}_2\text{Gd}_6$ alloy remains essentially unchanged, i.e. no additional phases form. The similar behavior has been observed during crystallization of amorphous $\text{Al}_{85}\text{Ni}_7\text{Gd}_8$ alloy [22] and has been interpreted as local chemical ordering which occurs in the residual amorphous matrix. Though the detailed analysis of the X-ray diffraction patterns has shown that the relative intensity of the fcc Al (111) and (200) reflections increases whereas their breadth decreases which indicates that growth of Al nanocrystals occurs at this crystallization stage. Heating to the end of the third stage induces of formation of one or more

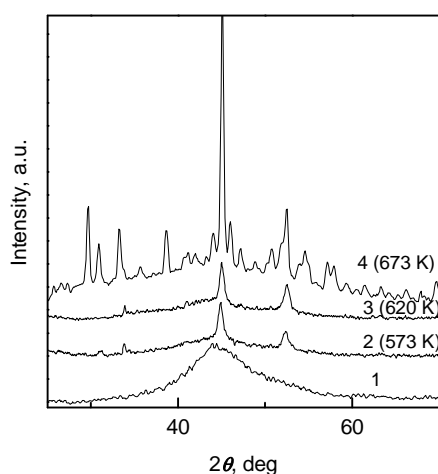
intermetallics (Fig. 5a) which structure has not yet been identified in the present study. The similar phase formation sequence has been also observed during crystallization of amorphous $\text{Al}_{86}\text{Ni}_6\text{Co}_2\text{Gd}_3\text{Y}_2\text{Tb}_1$ and $\text{Al}_{86}\text{Ni}_6\text{Fe}_2\text{Gd}_6$ alloys.

Table 2. Chemical composition, structure of the alloys after the first crystallization stage and activation energies.

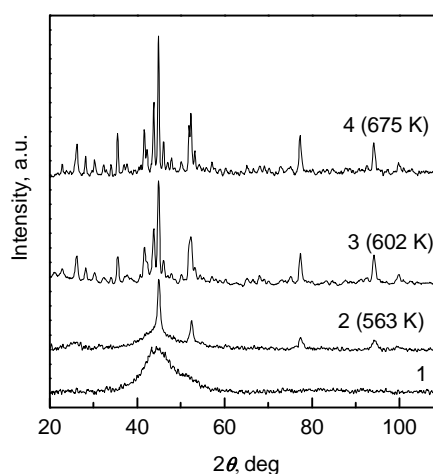
Alloy composition	No of casting run	Type of NC structure	Q_1 , K
$\text{Al}_{90}\text{Y}_{10}$	B-275	Al	22600 ± 200
$\text{Al}_{90}\text{Gd}_{10}$	B-272	Al	17000 ± 1600
$\text{Al}_{87}\text{Ni}_8\text{Y}_5$	B-112	Al	22700 ± 900
$\text{Al}_{87}\text{Ni}_8\text{Gd}_5$	B-252	Al	32100 ± 6200
$\text{Al}_{87}\text{Ni}_8\text{Gd}_1\text{Y}_4$	B-254	Al	24800 ± 1600
$\text{Al}_{86}\text{Ni}_6\text{Co}_2\text{Gd}_6$	B-276	Al	34300 ± 3500
$\text{Al}_{86}\text{Ni}_2\text{Co}_6\text{Gd}_6$	B-277	Al + IC	32800 ± 1200
$\text{Al}_{87}\text{Ni}_4\text{Fe}_4\text{Gd}_5$	B-251	Al	64700 ± 16200
$\text{Al}_{87}\text{Ni}_4\text{Fe}_4\text{Gd}_1\text{Y}_4$	B-257	Al	65800 ± 15600
$\text{Al}_{86}\text{Ni}_6\text{Fe}_2\text{Gd}_6$	B-287	Al	31000 ± 1900
$\text{Al}_{86}\text{Ni}_2\text{Fe}_6\text{Gd}_6$	B-289	Al+IC	28400 ± 6000

Somewhat different crystallization behavior has been established in a number of another amorphous alloys ($\text{Al}_{87}\text{Ni}_8\text{Gd}_5$, $\text{Al}_{87}\text{Ni}_8\text{Y}_5$, $\text{Al}_{87}\text{Ni}_8\text{Gd}_1\text{Y}_4$, $\text{Al}_{87}\text{Ni}_4\text{Fe}_4\text{Gd}_5$ and $\text{Al}_{87}\text{Ni}_4\text{Fe}_4\text{Gd}_5$) investigated where the second crystallization stage in amorphous corresponds to the formation of crystals one or several intermetallic phases as illustrated for $\text{Al}_{87}\text{Ni}_8\text{Gd}_5$ alloy in Fig. 5b. As can be seen in this Figure the positions of the peaks remain unchanged while they become somewhat narrower, i.e. growth of the phase precipitation is the main event at the third crystallization stage. These observations agree with the results reported in Ref. [23] for amorphous $\text{Al}_{87}\text{Ni}_8\text{Y}_5$ alloy where phases formed at the second crystallization stage were identified to be Al_3Ni and $\text{Al}_{23}\text{Ni}_6\text{Y}_4$. However, these data are in disagreement with those of Ref. [17], where for amorphous $\text{Al}_{87}\text{Ni}_8\text{Gd}_5$, $\text{Al}_{87}\text{Ni}_8\text{Y}_5$, $\text{Al}_{87}\text{Ni}_8\text{Gd}_1\text{Y}_4$, $\text{Al}_{87}\text{Ni}_4\text{Fe}_4\text{Gd}_5$ and $\text{Al}_{87}\text{Ni}_4\text{Fe}_4\text{Gd}_5$ alloys the phase formation sequence shown in Fig. 5a has been reported. One of the possible reasons of this controversy may be using of isothermal annealing in this study which may result in different crystallization path compared with that at constant rate heating [22].

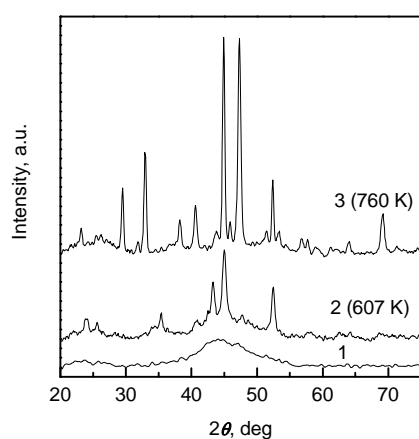
The last two studied amorphous $\text{Al}_{86}\text{Ni}_6\text{Co}_2\text{Gd}_6$ and $\text{Al}_{86}\text{Ni}_2\text{Fe}_6\text{Gd}_6$ alloys have a two-stage crystallization process (Fig. 5c) in which nanocrystals of Al together with another intermetallic phase(s) nanosized crystals form in the first stage (IC). These unidentified intermetallics are metastable and disappear in the second crystallization stage (Fig. 5c). Note that multi-phase crystallization behavior in the first stage has been observed in a number of the Al-based amorphous alloys (e.g., in $\text{Al}_{89}\text{La}_5\text{Ni}_5$ [24] and in $\text{Al}_{87}\text{Ni}_5\text{Co}_2\text{Nd}_6$ [16]) and it has been considered as eutectic crystallization. As it has been shown in Ref. [16] the change of the crystallization mode of the first stage is caused by partial replacement of Ni in amorphous $\text{Al}_{87}\text{Ni}_7\text{Nd}_6$ by Co. There have been only a few papers in the literature reporting the "eutectic" crystallization mode of Al-based glasses so both the kinetics and mechanism of this process are not established.



a)



b)



c)

Fig. 5. X-ray diffraction patterns of the as prepared (curves 1) melt-spun ribbons and heated up at 5 K/min to the end temperatures of first (curves 2), second (curves 4) and third (curves 4) crystallization stages indicated in the plots: (a) - $\text{Al}_{86}\text{Ni}_6\text{Co}_2\text{Gd}_6$; (b) - $\text{Al}_{87}\text{Ni}_8\text{Gd}_5$; (c) $\text{Al}_{86}\text{Ni}_2\text{Fe}_6\text{Gd}_6$.

Activity 2.2. Experimental studies of kinetics and mechanisms of nanocrystallization of amorphous Al-based alloys

As it has been shown in previous section there are several paths of crystallization process in the amorphous Al-based alloys investigated. In view of the essential improvement of the mechanical properties caused by formation of nanocomposite structures it is quite important to study the mechanisms of nanocrystallization. The most proper way to clarify the mechanism of the crystallization process includes the experimental studies of the process kinetics, structure of crystallized samples and analysis of the results within appropriate theoretical models.

Formation of nanocomposite structures occurs in the first crystallization stage of all amorphous alloys investigated, and in the majority cases they consist of Al nanocrystals embedded in residual amorphous matrix while in some cases (alloys enriched both in Co and Fe) nanoscale intermetallic compounds form simultaneously with Al as illustrated in Figures 6 and 7 respectively.

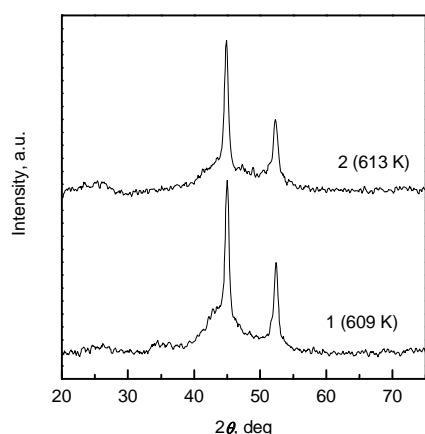


Fig. 6. X-ray diffraction patterns of the samples heated up at 5 K/min to temperatures of the first crystallization stage end: 1 – $\text{Al}_{87}\text{Ni}_4\text{Fe}_4\text{Gd}_5$, 2 – $\text{Al}_{87}\text{Ni}_4\text{Fe}_4\text{Gd}_1\text{Y}_4$.

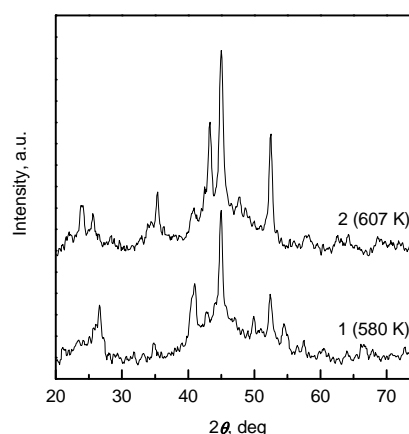


Fig. 7. X-ray diffraction patterns of the samples heated up at 5 K/min to temperatures of the first crystallization stage end: 1 – $\text{Al}_{86}\text{Ni}_2\text{Co}_6\text{Gd}_6$, 2 – $\text{Al}_{86}\text{Ni}_2\text{Fe}_6\text{Gd}_6$.

To clarify the features of kinetics of these two types of nanocrystallization the volume fractions of crystalline phases, X , have been determined from the X-ray diffraction patterns of the samples heated up to temperatures of the end of the first crystallization stage (similar to those shown in Figs. 6 and 7) and the experimentally measured changes of relative electrical resistance $R(T)/R_0$ have been converted into the kinetic nanocrystallization curves $X(T)$. For better visualization the $X(T)$ curves were numerically differentiated and such obtained dependencies of the nanocrystallization rate on temperature (similar to DSC scans [8]) are shown in Figures 8 and 9.

The common feature of all curves is the tails observed at high temperature sides of the nanocrystallization rate peaks which is typical for the first crystallization stage of amorphous Al-based alloys [25]. However, in the case of multi-phase nanocrystallization the rate of transformation increases by step-wise manner (curves 3 in Figs. 8, 9) while rate of formation of Al nanocrystals increases with temperature gradually. Note that similar changes of the maxima of the heat flow corresponding to the first crystallization stage resulted from partial replacement of Ni with Co have been observed at the DSC thermograms of amorphous $\text{Al}_{87}\text{Ni}_{8-x}\text{Co}_x\text{La}_5$ alloys [15].

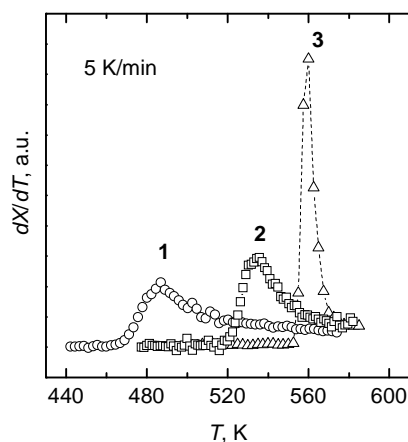


Fig. 8. Effect of partial replacement of Ni with Co on the rate of the first stage of crystallization of the Al-based amorphous alloys at 5 K/min: 1 – $\text{Al}_{86}\text{Ni}_6\text{Co}_2\text{Gd}_6$; 2 – $\text{Al}_{86}\text{Ni}_4\text{Co}_4\text{Gd}_6$; 3 – $\text{Al}_{86}\text{Ni}_2\text{Co}_6\text{Gd}_6$.

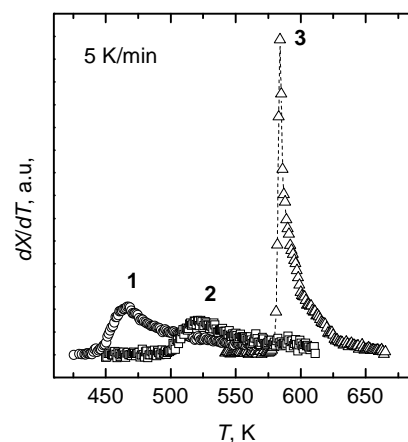


Fig. 9. Effect of partial replacement of Ni with Fe on the rate of the first stage of crystallization of the Al-based amorphous alloys at 5 K/min: 1 – $\text{Al}_{87}\text{Ni}_8\text{Gd}_5$; 2 – $\text{Al}_{87}\text{Ni}_4\text{Fe}_4\text{Gd}_5$; 3 – $\text{Al}_{86}\text{Ni}_2\text{Fe}_6\text{Gd}_6$.

For more detailed analysis of mechanisms of nanocrystallization the studies of isothermal crystallization kinetics at different annealing temperatures have been performed. Several examples of the isothermal kinetic crystallization curves, $X(t)$, obtained from the measurements of the electrical resistance changes of the amorphous alloys with various nanocrystallization modes are shown in Fig. 10. As it can be seen from this data in the case of nanocrystallization of Al (Fig. 10 a,b) the crystallized volume fraction increases with time with saturation, whereas in the case of multi-phase nanocrystallization (Fig 10c) $X(t)$ changes sigmoidally. The former behavior of $X(t)$ is typical not only for nanocrystallization of many amorphous Al-based alloys, but also for the nanocrystal forming Fe-based FINEMET alloys (e.g., [26-28]) and it is assumed to be related with lowering of the rate of crystal growth. On the contrary, the sigmoidal shape of the kinetic curve of multi-phase nanocrystallization is typical for the majority of the metallic glasses [29] crystallizing into structures with relatively coarse grain size.

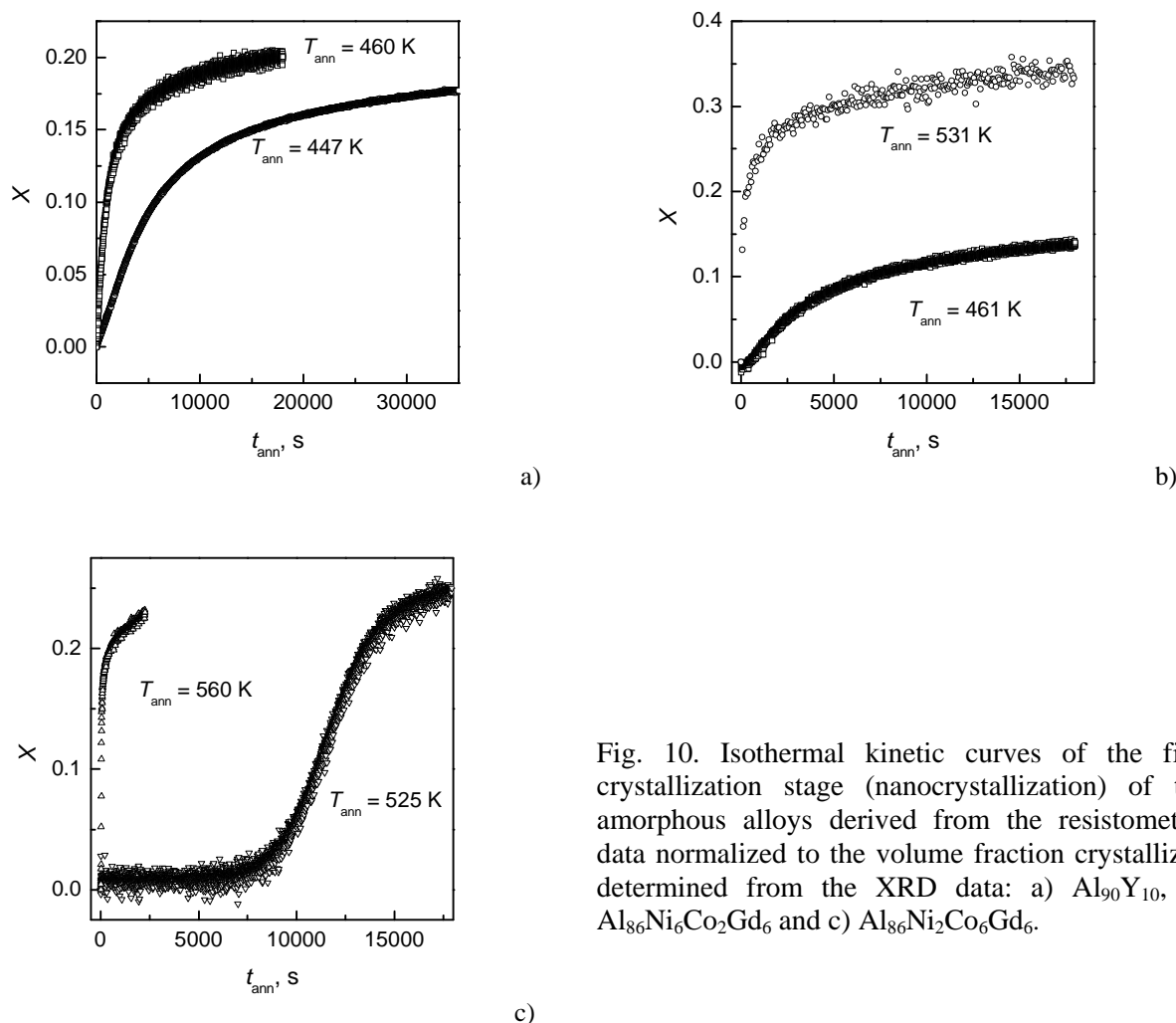


Fig. 10. Isothermal kinetic curves of the first crystallization stage (nanocrystallization) of the amorphous alloys derived from the resistometric data normalized to the volume fraction crystallized determined from the XRD data: a) $\text{Al}_{90}\text{Y}_{10}$, b) $\text{Al}_{86}\text{Ni}_6\text{Co}_2\text{Gd}_6$ and c) $\text{Al}_{86}\text{Ni}_2\text{Co}_6\text{Gd}_6$.

The experimentally measured kinetic crystallization curves $X(t)$ have been used to obtain information the possible nanocrystallization mechanisms within the commonly used for this purpose classical Kolmogorov-Johnson-Mehl-Avrami (KJMA) theory [30]. This theory describes the transformed under isothermal conditions volume fraction on time as $X(t) = 1 - \exp(-Kt^n)$ with K being the kinetic constant. The so-called Avrami exponent, n , characterizes the dimensionality of the transformation and depends on whether the transformation is interface or diffusion controlled and on the nucleation rate. In order to estimate the values of n the kinetics crystallization curves shown in Fig. 10 have been plotted as $\ln[-\ln(1 - X)]$ versus $\ln(t)$. The common feature of the plots presented in Figures 11–13 for the alloys investigated (as well as for the amorphous nanocrystals forming Al- and Fe-based alloys [27,28]) is considerable deviation from straight lines

pointing to the failure of the KJMA equation or at least to its applicability only to the initial stage of nanocrystallization. The theoretical analysis of the nanocrystallization process has shown that the gradual lowering of the Avrami exponent in the course of transformation may be caused with blocking of the nanocrystals growth [27,28], which is not accounted for in the KJMA model. Nevertheless, the data presented in Figures 11–13 allow making several assumptions about mechanisms of nanocrystallization in the amorphous Al-based alloys investigated.

As shown in Fig. 11, the slopes of the straight lines provide an Avrami exponent of 1 for initial stages of Al-nanocrystals formation in amorphous Al₉₀Y₁₀ alloy at different annealing temperatures. In the light of generally accepted interpretation [30] this value of n corresponds to two-dimensional diffusion controlled growth. Note, that similar value of n has been found for amorphous Al₈₈La₂Gd₆Ni₄ in which three-dimensional diffusion-controlled growth of Al nanocrystals has been established by microstructural analysis [27]. In view, that value of $n = 1$ for Al₉₀Y₁₀ alloy has been found for different annealing temperatures (Fig. 11) this result allows suggestion that nanocrystallization of this amorphous alloy occurs by diffusion-controlled growth of the pre-existing (the most probably quenched-in) Al nuclei the high density of which retards the grain growth during the crystallization process.

In contrast to Al₉₀Y₁₀ alloy the value of Avrami exponent at initial stages of nanocrystallization of amorphous Al₈₆Ni₆Co₂Gd₆ alloy is strongly dependent on annealing temperature and is found to be 2.6 and 0.26 at 461 and 501 K, respectively (Fig. 12). The former value of n is close to 2.5 which indicates diffusion-limited growth with steady-state nucleation [30]. Note, that this crystallization mechanism has been identified experimentally in amorphous Al₈₅Ni₅Y₈Co₂ alloy [8] where, in part, has been established that nucleation of Al nanocrystals takes place only at initial stage of the process. It assumes that lowering n with temperature in this alloy may be caused by retardation of both the nucleation and growth processes. While retardation of growth may be result from impingement of the diffusion fields, the blocking of nucleation may be caused by the increase of the total concentration of alloying elements in the residual amorphous matrix which hinders the formation of pure Al nuclei. To validate the suggested nanocrystallization mechanism of amorphous Al₈₆Ni₆Co₂Gd₆ alloy it is necessary to estimate the parameters of nanocomposite structures obtained at different temperatures and this results will be presented in the next section.

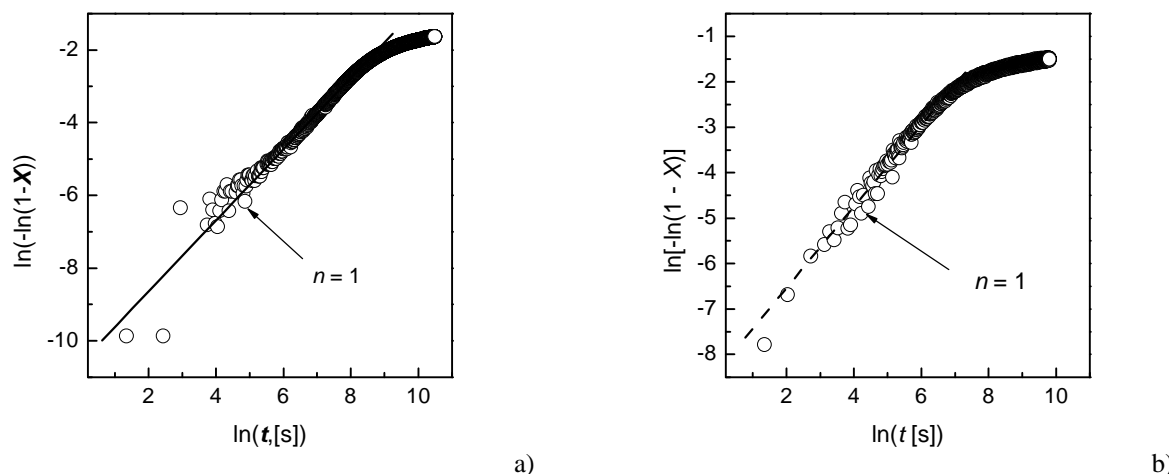


Fig. 11. Avrami plots for amorphous Al₉₀Y₁₀ alloy from the data presented in Fig. 10(a) for annealing temperatures 447 K (a) and 460 K (b).

In contrast to Al₉₀Y₁₀ alloy the value of Avrami exponent at initial stages of nanocrystallization of amorphous Al₈₆Ni₆Co₂Gd₆ alloy is strongly dependent on annealing temperature and is found to be 2.6 and 0.26 at 461 and 501 K, respectively (Fig. 12). The former value of n is close to 2.5 which indicates diffusion-limited growth with steady-state nucleation [30]. Note, that this crystallization mechanism has been identified experimentally in amorphous Al₈₅Ni₅Y₈Co₂ alloy [8] where, in part, has been established that nucleation of Al nanocrystals takes place only at initial stage of the process. It assumes that lowering n with temperature in this alloy may be caused by retardation of both the nucleation and growth processes. While retardation of growth may be result from impingement of the diffusion fields, the blocking of nucleation may be caused by the

increase of the total concentration of alloying elements in the residual amorphous matrix which hinders the formation of pure Al nuclei. To validate the suggested nanocrystallization mechanism of amorphous $\text{Al}_{86}\text{Ni}_6\text{Co}_2\text{Gd}_6$ alloy it is necessary to estimate the parameters of nanocomposite structures obtained at different temperatures and this results will be presented in the next section.

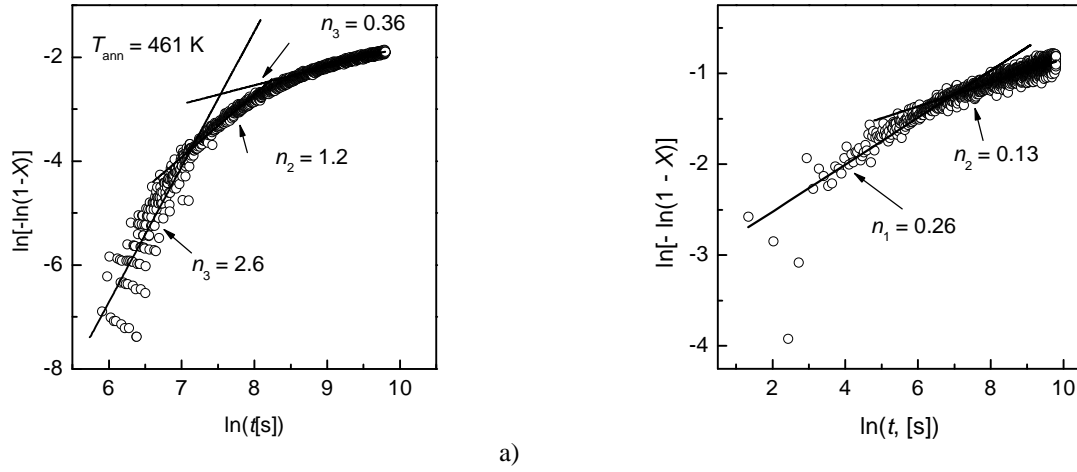


Fig. 12. Avrami plots for amorphous $\text{Al}_{86}\text{Ni}_6\text{Co}_2\text{Gd}_6$ alloy from the data presented in Fig. 6 (b) for annealing temperatures 461 K (a) and 501 K (b).

The appreciably higher values of the Avrami exponents have been found for the initial stages of nanocrystallization of amorphous $\text{Al}_{86}\text{Ni}_6\text{Co}_2\text{Gd}_6$ alloy where intermetallic compound(s) crystallizes simultaneously with Al (Fig. 13). As can be seen the value of n has a tendency to lowering with annealing temperature from 5.6 to 4. The latter value of n corresponds the case of interface controlled crystallization with constant rates of crystal nucleation and three-dimensional growth, while $n > 4$ indicates of transient nucleation with increasing frequency [30]. At first sight, these estimations are in agreement with supposed above eutectic crystallization mechanism for amorphous $\text{Al}_{86}\text{Ni}_2\text{Co}_6\text{Gd}_6$ and $\text{Al}_{86}\text{Ni}_2\text{Fe}_6\text{Gd}_6$ alloys similar to that identified for alloy $\text{Al}_{89}\text{La}_6\text{Ni}_5$ [24]. However, both lowering of n in the course of multi-phase crystallization and lack in the literature of microstructural studies of the partially crystallized samples leave the proposed eutectic mechanism of this process not clear identified.

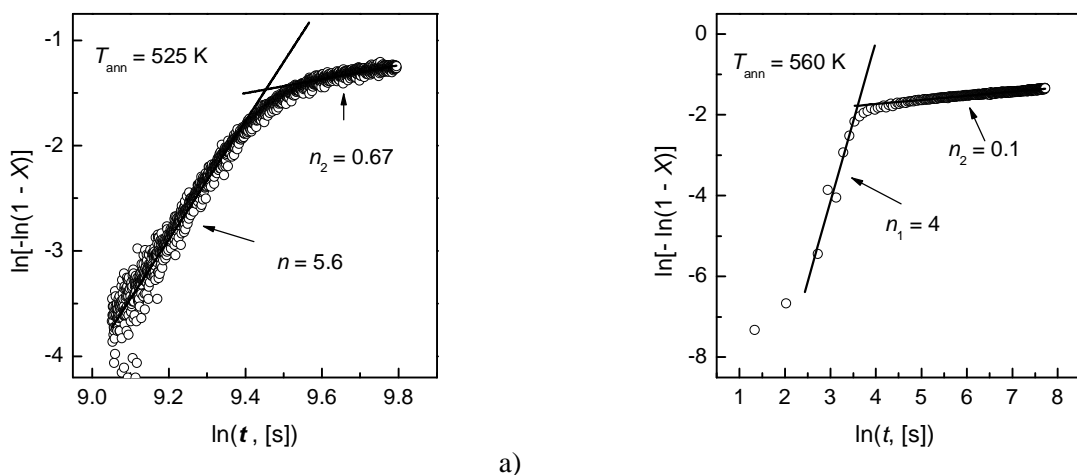


Fig. 13. Avrami plots for amorphous $\text{Al}_{86}\text{Ni}_2\text{Co}_6\text{Gd}_6$ alloy from the data presented in Fig. 6(c) for annealing temperatures 525 K (a) and 560 K (b).

To summarize this section it can be said that analysis of nanocrystallization kinetics of the amorphous alloys reveals several underlying mechanisms: (i) diffusion-controlled growth of the pre-existing Al nuclei ($\text{Al}_{90}\text{Y}_{10}$), (ii) nucleation and diffusion-limited growth of Al nanocrystals ($\text{Al}_{86}\text{Ni}_6\text{Co}_2\text{Gd}_6$), and (iii) eutectic-like transformation by transient nucleation and interface controlled growth of nanocrystals of Al and intermetallic

compound(s) ($\text{Al}_{86}\text{Ni}_2\text{Co}_6\text{Gd}_6$). Further work is required to understand the origin of lowering of Avrami exponent in the course of nanocrystallization as well as to establish the possible mechanisms of nucleation.

Activity 2.3 Determination of the parameters of nanocomposite structures as a function of alloy chemical composition and thermal prehistory of the amorphous Al-based alloys

As it has been shown above (Figs. 5–7) a general microstructural feature of the investigated amorphous Al-TM-RE alloys after the first crystallization stage is presence of nanoscale crystals of Al (in some cases with intermetallics) in a residual amorphous matrix. As it is known from the literature [2–4, 26, 31–33] formation of such nanocomposite structures leads to essential strengthening of Al-based alloys which is of practical importance. Despite the strengthening mechanisms in such nanocomposite structures are controversial [4, 26, 32], it is established that mechanical properties are strongly dependent on the crystallized volume fraction while the effects of the size and volume density of Al nanocrystals have not been studied. In order to elucidate these effects the influence of the chemical composition and the heat treatment regimes on the size and volume density of Al nanocrystals have been studied.

The volume fraction of nanocrystalline Al has been estimated in the samples heated up the end of the first crystallization stage from the X-ray diffraction patterns similar to those shown in Figs. 6 and 7 using Eq. 2. Size of Al nanocrystals have been calculated from the Sherrer formula $L = 0.9\lambda/(B_\theta \cos\theta_B)$, where B_θ is the breadth (full width at half-maximum) of the (111) peak and θ_B is the angular position of the center of the peak. In turn, using the values of these parameters the volume densities of Al nanocrystals have calculated as $N = 6X/(\pi L^3)$. Such estimated values of the structural parameters of nanocomposites are listed in Table 3. Note, that in the case of formation more that one nanocrystalline phase the total volume of the crystalline phases has been calculated from Equation (1). These compositions are marked by * in Table 3.

As it can be seen, the crystallized volume fractions, the average sizes of Al nanocrystals and their densities formed in the first crystallization event are in the ranges (0.22–0.59), (14.8–21.0) nm and $(1.1–4.3)\times 10^{23} \text{ m}^{-3}$, respectively. The lattice parameters of fcc Al nanocrystals have been found to be about 0.450 nm in all samples with nanocomposite structure which coincides with that of pure Al. These values are in general agreement with those found in other Al-based alloys with nanocomposite structure (e.g., [8, 26, 34]). We have note here that any systematic correlation between the chemical composition of the amorphous alloys and the nanophase composite parameters is not evident.

Table 3. Chemical composition, structural parameters of nanophase composites, their microhardness and its increment after the first crystallization stage of continuously heated samples.

Alloy composition	No of casting run	L , nm	X	N , m^{-3}	H_μ after I stage, MPa	ΔH_μ , MPa
$\text{Al}_{90}\text{Y}_{10}$	B-275	15.7	0.4	2×10^{23}	3950	1700
$\text{Al}_{87}\text{Ni}_8\text{Y}_5$	B-112	20.1	0.59	1.4×10^{23}	5200	1720
$\text{Al}_{87}\text{Ni}_8\text{Gd}_5$	B-252	15.6	0.38	3.5×10^{23}	5180	2130
$\text{Al}_{87}\text{Ni}_8\text{Gd}_1\text{Y}_4$	B-254	14.8	0.32	3.5×10^{23}	4880	1740
$\text{Al}_{86}\text{Ni}_6\text{Co}_2\text{Gd}_6$	B-276	15.6	0.44	2.2×10^{23}	4360	1000
$\text{Al}_{86}\text{Ni}_2\text{Co}_6\text{Gd}_6$ *)	B-277	15.4	0.22	1.1×10^{23}	5100	1630
$\text{Al}_{87}\text{Ni}_4\text{Fe}_4\text{Gd}_5$	B-251	18.7	0.41	2.2×10^{23}	4890	1430
$\text{Al}_{87}\text{Ni}_4\text{Fe}_4\text{Gd}_1\text{Y}_4$	B-257	16.4	0.51	4.3×10^{23}	4830	1400
$\text{Al}_{86}\text{Ni}_6\text{Fe}_2\text{Gd}_6$	B-287	20.6	0.25	1.1×10^{23}	4120	740
$\text{Al}_{86}\text{Ni}_2\text{Fe}_6\text{Gd}_6$ *)	B-289	16.3	0.31	2×10^{23}	4940	1380

*) Multiphase structure

In order to study the effect of the heat treatment regime on the parameters of nanophase composites amorphous $\text{Al}_{90}\text{Y}_{10}$, $\text{Al}_{87}\text{Ni}_4\text{Fe}_4\text{Gd}_5$ and $\text{Al}_{86}\text{Ni}_6\text{Co}_2\text{Gd}_6$ ribbons has been isothermally annealed to the end of the first crystallization stage (for 1800 s at 460 K, for 18000 s at 557 K and for 79200 s at 433 K, respectively). The results of the calculations are listed in Table 4. It is evident that structural parameters of nanophase composites in $\text{Al}_{90}\text{Y}_{10}$ and $\text{Al}_{87}\text{Ni}_4\text{Fe}_4\text{Gd}_5$ alloys are practically independent on thermal regime of heat treatment whereas long term annealing of amorphous $\text{Al}_{86}\text{Ni}_6\text{Co}_2\text{Gd}_6$ alloy leads to formation of essentially smaller nanocrystals with higher volume density in comparison with those formed at constant rate

heating. These results suggests that the nucleation process plays an important role in the primary crystallization of $\text{Al}_{86}\text{Ni}_6\text{Co}_2\text{Gd}_6$ alloy in contrast to the $\text{Al}_{90}\text{Y}_{10}$ and $\text{Al}_{87}\text{Ni}_4\text{Fe}_4\text{Gd}_5$ alloys which crystallize presumably by the diffusion limited growth of the "quenched-in" nuclei.

Table 4. Comparison of the parameters of nanocomposite structures obtained at isothermal conditions and at continuous heating

Alloy composition	No of casting run	$X_{1(\text{iso})}$	$X_{1(\text{heat})}$	L_{iso} , nm	L_{heat} , nm	N_{iso} , m^{-3}	N_{heat} , m^{-3}
$\text{Al}_{90}\text{Y}_{10}$	B-275	0.45	0.4	17.3	17.9	1.7×10^{23}	1.3×10^{23}
$\text{Al}_{87}\text{Ni}_4\text{Fe}_4\text{Gd}_5$	B-251	0.33	0.41	15.6	18.7	3.1×10^{23}	2.2×10^{23}
$\text{Al}_{86}\text{Ni}_6\text{Co}_2\text{Gd}_6$	B-276	0.58	0.44	8.5	15.6	1.8×10^{24}	2.2×10^{23}

It should be noted that the results presented in this section are preliminary and to make the reliable conclusion the systematic studies of the influence of both temperature of isothermal annealing and rate of heating on the parameters of nanocomposite structures will be carried out.

Besides, it was of interest to examine the effect of nanocrystallization on the microhardness of the partially crystallized amorphous alloys. From the results presented in Fig. 14 for two binary alloys it is seen that formation of Al nanocrystals results in essential enhancement of microhardness while crystallization of intermetallic phases leads to lowering of H_μ which is typical for amorphous Al-TM-RE alloys [3, 4, 33]. The maximum values of H_μ which reached at the end of the first crystallization stage of the alloys investigated at constant rate heating are listed in Table 3 together with the microhardness increments caused by nanocrystallization. The highest values of H_μ (about 5200 MPa) and very high its increments (> 1700 MPa) were found in the ternary $\text{Al}_{87}\text{Ni}_8\text{Y}_5$ and $\text{Al}_{87}\text{Ni}_8\text{Gd}_5$ alloys with nanocomposite structures. It is somewhat surprising that both H_μ and ΔH_μ in multiphase nanocomposite structures containing intermetallics in $\text{Al}_{86}\text{Ni}_2\text{Co}_6\text{Gd}_6$ and $\text{Al}_{86}\text{Ni}_2\text{Fe}_6\text{Gd}_6$ alloys do not exceed those in the partially crystallized alloys containing only Al nanocrystals. It is not yet possible, however, to establish clear correlations between the hardness of nanophase composites obtained at continuous heating and both their structural parameters and chemical compositions except a tendency for H_μ to increase with increasing of the density Al nanocrystals and due to partial replacement of Ni with Co or Fe. The H_μ values of nanophase composite structures formed in $\text{Al}_{87}\text{Ni}_8\text{Y}_5$, $\text{Al}_{87}\text{Ni}_8\text{Gd}_5$ and $\text{Al}_{86}\text{Ni}_2\text{Co}_6\text{Gd}_6$ alloys (Table 3) are close to the highest values of that found for $\text{Al}_{88}\text{Ni}_4\text{Y}_8$ ($\sim 530 \text{ kgf/mm}^2$) [26] and $\text{Al}_{89}\text{Ni}_6\text{La}_6$ (about 540 kgf/mm^2) [35].

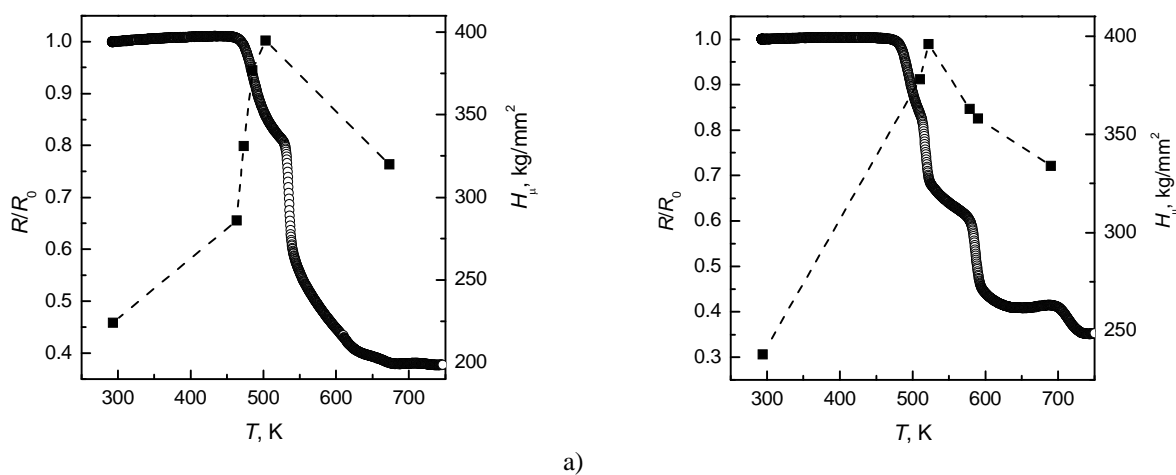


Fig. 14. Effect of crystallization on microhardness (right axis) of amorphous $\text{Al}_{90}\text{Y}_{10}$ (a) and $\text{Al}_{90}\text{Gd}_{10}$ (b) alloys.

The detailed investigations of correlations between the mechanical properties of nanocomposite structures and their structural parameters will be performed at the final stage of the project.

Activity 2.4. Studies of the temperature/time limits of stability of nanocomposite structure in the Al-based alloys

It follows from the above (Table 3) that the partially crystallized Al-based alloys with nanocomposite structure which formed at the first crystallization stage have the most attractive potential for structural applications. However, the nanocomposite structure is thermodynamically metastable and subsequent crystallization which takes place at higher temperatures at continuous heating results in the pronounced lowering of the hardness (Fig. 14). It indicates that the studies of kinetics and mechanism of the second crystallization stage are very important for development of high-strength Al-based alloys for elevated temperature applications as well as for estimation of the temperature ranges of consolidation processing of rapidly quenched materials. However, until now the second crystallization stage in Al-based amorphous alloys has been not studied at the proper level (e.g., [35,36]).

As in the case of amorphous phases thermal stability of nanophase composites in the present study has been characterized by the onset crystallization temperature of the second crystallization stage, T_{ons2} , measured at constant rate heating which has been estimated from the curves $R(T)/R_0$ similar to that as T_{ons1} (Fig. 1). Such determined values of T_{ons2} for the alloys investigated listed in Table 5 are in the relatively wide range of temperatures from 520 K (for Al₉₀Y₁₀ alloy) to 619 K (for Al₈₇Ni₄Fe₄Gd₁Y₄ alloy). In contrast to the temperatures of first crystallization onset, T_{ons1} , (Section 2.1) there is no well pronounced correlation between the chemical composition of the alloys and thermal stability of nanocomposite structures.

Table 5. Chemical composition, number of casting run and the parameters of thermal stability of amorphous and nanocomposite alloys

	Alloy composition	No of casting run	Number of stages	T_{ons1} , K	T_{ons2} , K	ΔT , K	Q_2 , K
1	Al ₉₀ Y ₁₀	B-275	2	464 ± 1	520 ± 1	56	22100 ± 1200
2	Al ₈₇ Ni ₈ Y ₅	B-112	3	484 ± 1	579 ± 1	95	-
3	Al ₈₇ Ni ₈ Gd ₅	B-252	3	453 ± 1	579 ± 1	126	33000 ± 1200
4	Al ₈₇ Ni ₈ Gd ₁ Y ₄	B-254	3	440 ± 1	583 ± 1	143	30200 ± 3010
5	Al ₈₆ Ni ₆ Co ₂ Gd ₆	B-276	3	501 ± 1	584 ± 1	83	29300 ± 1100
6	Al ₈₆ Ni ₂ Co ₆ Gd ₆	B-277	2	545 ± 1	594 ± 1	49	25000 ± 2000
7	Al ₈₇ Ni ₄ Fe ₄ Gd ₅	B-251	3	506 ± 1	617 ± 1	111	43900 ± 7800
8	Al ₈₇ Ni ₄ Fe ₄ Gd ₁ Y ₄	B-257	3	497 ± 1	619 ± 1	122	29900 ± 820
9	Al ₈₆ Ni ₆ Fe ₂ Gd ₆	B-287	3	509 ± 1	590 ± 1	81	-
10	Al ₈₆ Ni ₂ Fe ₆ Gd ₆	B-289	2	584 ± 1	596 ± 1	12	11100±1700

Another important parameter of alloys with nanocomposite structure from point of view their subsequent warm consolidation by pressing (e.g., [7]) is difference between the temperatures of the onset of the second and first crystallization stages ($\Delta T = T_{ons2} - T_{ons1}$). This parameter determines the temperature range in which the consolidation process can be carried out without degradation of the enhanced mechanical properties. As it is evident from Table 5 the largest values of ΔT (143, 126 and 122 K) have been found in Al₈₇Ni₈Gd₁Y₄, Al₈₇Ni₈Gd₅ and Al₈₇Ni₄Fe₄Gd₁Y₄ alloys, respectively.

For further characterization of the second crystallization stage the effective activation energy, Q_2 have been determined using the Kissinger technique [19] as it is shown in Fig. 15. The apparent activation energies of the second crystallization stage are in the range from 11100 to 43900 K (Table 5) and there is no clear correlation between the values of Q_2 and thermal stability of nanocomposite structures. It is of interest to note that practically all values of Q_2 which characterizes crystallization of intermetallic compounds are lower than the activation energies of the first crystallization stage (Table 1). It, in particular, may be caused by enrichment of the remaining amorphous matrix by solute atoms such facilitating nucleation of intermetallics. Note, that the reported value of the apparent activation energy of the second crystallization stage 18400 ± 640 K [36] (formation of Al₁₁(La,Ce)₃ phase) in amorphous Al_{87.5}Ni₇Mm₅Fe_{0.5} alloy is in the range of Q_2 values presented in Table 5.

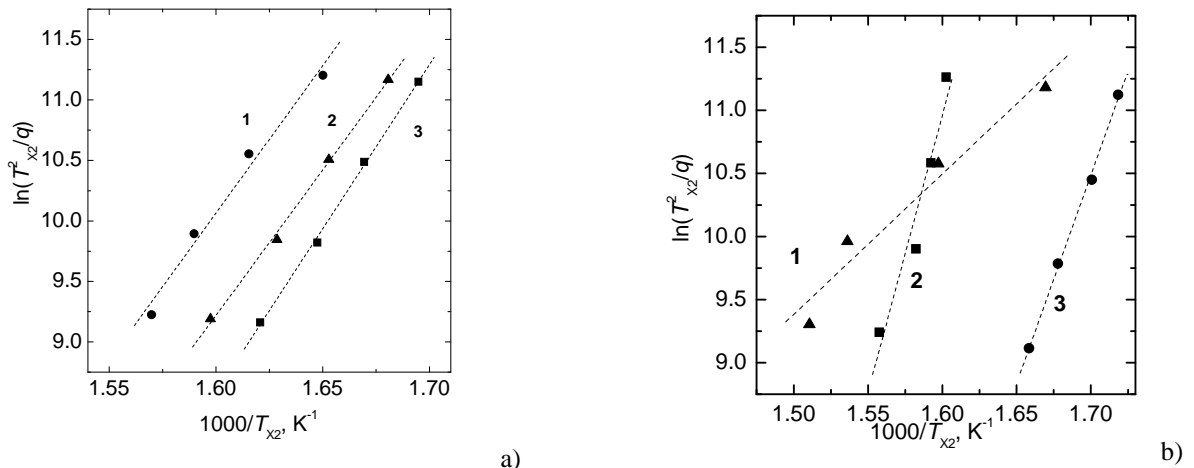


Fig. 15. Kissinger plots derived from crystallization peak temperatures, T_{X2} , for the amorphous alloys: (a) 1 – $\text{Al}_{86}\text{Ni}_2\text{Co}_6\text{Gd}_6$ (circles), 2 – $\text{Al}_{86}\text{Ni}_4\text{Co}_4\text{Gd}_2\text{Y}_4$ (triangles), 3 – $\text{Al}_{86}\text{Ni}_6\text{Co}_2\text{Gd}_6$ (squares); (b) 1 – $\text{Al}_{86}\text{Ni}_2\text{Fe}_6\text{Gd}_6$ (triangles), 2 – $\text{Al}_{87}\text{Ni}_4\text{Fe}_4\text{Gd}_5$ (squares), 3 – $\text{Al}_{87}\text{Ni}_8\text{Gd}_5$ (circles).

For better understanding of kinetics of the second crystallization stage the samples of two amorphous alloys $\text{Al}_{90}\text{Y}_{10}$ and $\text{Al}_{86}\text{Ni}_6\text{Co}_2\text{Gd}_6$ have been annealed at temperatures somewhat lower than $T_{\text{ons}2}$ to observe two crystallization stages in one experiment. As can be seen in Fig. 16 both crystallization stages are clearly revealed by two separate drops in electrical resistance. For estimation of the crystallized volume fractions at each crystallization stage (X_1 and X_2) the X-ray diffraction patterns of the samples annealed to the end of the first and second crystallization stages (similar to those presented in Figs. 2 and 5) have been used. The values of X_1 and X_2 determined using Eq. 2 were used for transformation of the $R(t)$ curves to kinetic crystallization curves $X(t)$ shown in Fig. 16 (right axes).

As it is evident from the X-ray diffraction data the sample of $\text{Al}_{90}\text{Y}_{10}$ alloy is fully crystallized after second crystallization stage (Fig. 2) while the X-ray diffraction patterns of the $\text{Al}_{86}\text{Ni}_6\text{Co}_2\text{Gd}_6$ sample after first and second crystallization stages are similar (cf. curves 2 and 3 in Fig. 5). As it has been discussed above (Section 2.1) the similar crystallization behavior for amorphous $\text{Al}_{85}\text{Ni}_7\text{Gd}_8$ alloy was interpreted as local chemical ordering occurring in the remaining amorphous matrix [22]. However, this explanation seems to be ambiguous accounting the appreciable drop in the resistance and well defined separation between the first and second crystallization stages at continuous heating (Fig. 3c) and isothermal annealing (Fig. 16b). Besides, the value of the average size of the Al nanocrystals after the second crystallization event estimated from the X-ray diffraction pattern presented in Fig. 5a (curve 3) is about 19.6 nm, i.e. 4 nanometers higher than formed at the first crystallization stage (Table 3).

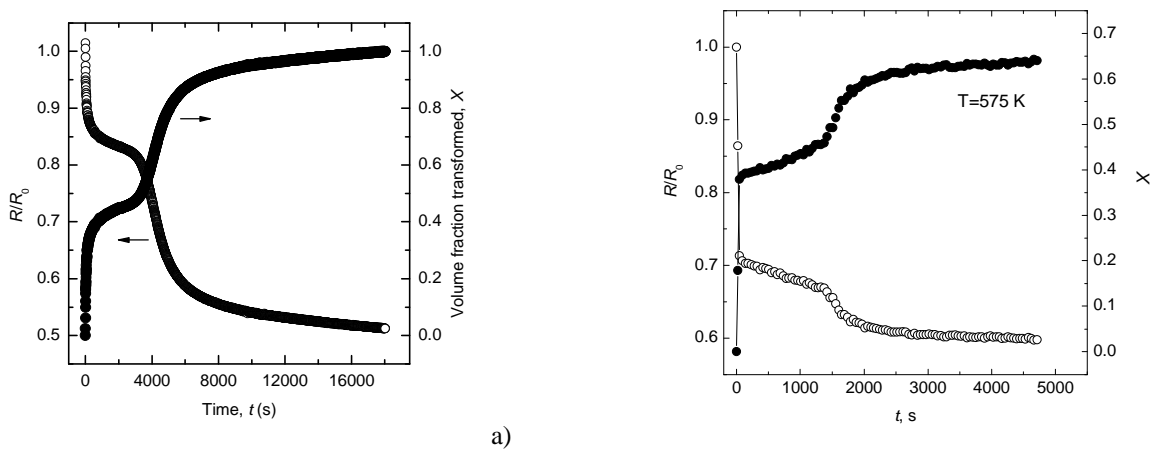


Fig. 16. Changes of the relative electrical resistance (left axis) and the volume fraction transformed (right axis) under isothermal annealing of amorphous alloys (a) $\text{Al}_{90}\text{Y}_{10}$ at 487 K and (b) $\text{Al}_{86}\text{Ni}_6\text{Co}_2\text{Gd}_6$ at 575 K.

The isothermal two-stage crystallization curves $X(T)$ of amorphous $\text{Al}_{86}\text{Ni}_6\text{Co}_2\text{Gd}_6$ and $\text{Al}_{90}\text{Y}_{10}$ alloys shown in Fig. 16 were transformed to the Avrami plots (Fig. 17). As can be seen from Fig. 17 the second crystallization stage is also well pronounced in these plots. Besides, these plots at each crystallization stage are not linear which indicates that the processes do not follow the KJMA kinetic equation. Though, from results of linearization of the initial stages of the second crystallization stage (shown by dash lines) some assumptions about transformation mechanisms may be done. In fact, the slope $n_2 = 2.5$ for the second (final) stage of crystallization of amorphous $\text{Al}_{90}\text{Y}_{10}$ corresponds to the process which occurs by steady state nucleation and diffusion-limited growth. This is in general agreement with the X-ray diffraction data (Fig. 2, Table 3) which show that in this crystallization stage formation of Al_3Y intermetallic compound from the residual amorphous matrix enriched in Y as well coarsening of the Al nanocrystals takes place. In any case both these processes require redistribution of the Al and Y atoms, so the assumed crystallization mechanism seems reasonable.

The Avrami exponent $n_2 = 1.3$ established for the second crystallization stage of amorphous $\text{Al}_{86}\text{Ni}_6\text{Co}_2\text{Gd}_6$ alloy is comparable and even somewhat higher than that for the first crystallization stage (Fig. 17b) where the diffusion-limited growth of Al nanocrystals is dominating process. Therefore, the similar crystallization mechanism may be assumed for the second crystallization stage of $\text{Al}_{86}\text{Ni}_6\text{Co}_2\text{Gd}_6$ alloy which, however, needs in subsequent verification.

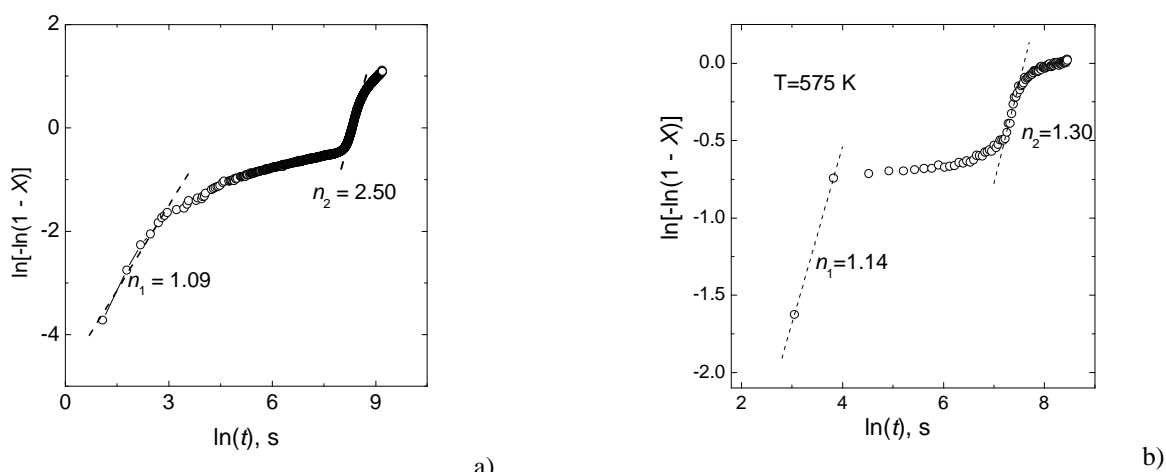


Fig. 17. Avrami plots for isothermal two stage crystallization of (a) $\text{Al}_{90}\text{Y}_{10}$ at 487 K and (b) $\text{Al}_{86}\text{Ni}_6\text{Co}_2\text{Gd}_6$ at 575 K from the data presented in Fig. 16.

In conclusion, it should be noted, that the second crystallization stage in the majority of the Al-based alloys investigated begins at temperatures above 573 K (Table 3) which indicates that the materials with nanocomposite structure may be considered as potential candidates for elevated temperature applications.

Activity 2.5. Development of theoretical models of nanocrystallization at isothermal conditions and upon constant rate heating and comparison with the experimental data

As it has been established above (Section 2.2) kinetics of formation nanophase composites in amorphous Al-based alloys does not follow the classical KJMA formalism which is widely used for description of glass crystallization including the primary mode [29]. The progressive lowering of the Avrami exponent in the course of nanocrystallization (Figs. 8, 9) which is apparent from the tails observed at high temperature side of the peaks in the dX/dT vs. T (Figs. 11–13) curves indicates that the rate of the process is reduced due to internal reasons. In turn, it may be caused by lowering of the rates of crystal nucleation and growth. In view of an ultra-high density of order 10^{23} m^{-3} of Al-nanocrystals it has been proposed [25] that the slowing down of the nanocrystallization results from growth limitations which is caused by impingement of the diffusion fields enriched in atoms of TM and RE components rejected from growing nanocrystals. This diffusion-field impingement was detected experimentally in amorphous $\text{Al}_{87}\text{Ni}_{10}\text{Ce}_3$ alloy [37] and main efforts have been concentrated on developing of the theoretical approaches to describe this effect [28]. The majority of these models are numerical or semi-quantitative which complicates their using for interpreting of experimental data. On the other hand, it has been shown [25] that the primary crystallization kinetics of amorphous $\text{Al}_{88}\text{Ni}_{17}\text{Y}_5$

alloy may be satisfactory described by using of the exact analytical solution developed by Ham for the growth of the array of precipitation in supersaturated solid solution [38]. However the expressions obtained by Ham are too cumbersome to be used conveniently. In view that the properties of materials with nanocomposite structure are strongly dependent on the size and density of the nanocrystals it is highly desired to develop a relatively simple analytical model to identify the main parameters governing the nanocrystallization process as well as to estimate their values.

In order to simplify description of the diffusion-limited growth of crystals accounting the diffusion fields an attempt to obtain the approximate solution of the problem solved by Ham (Fig. 18) has been recently made [39].

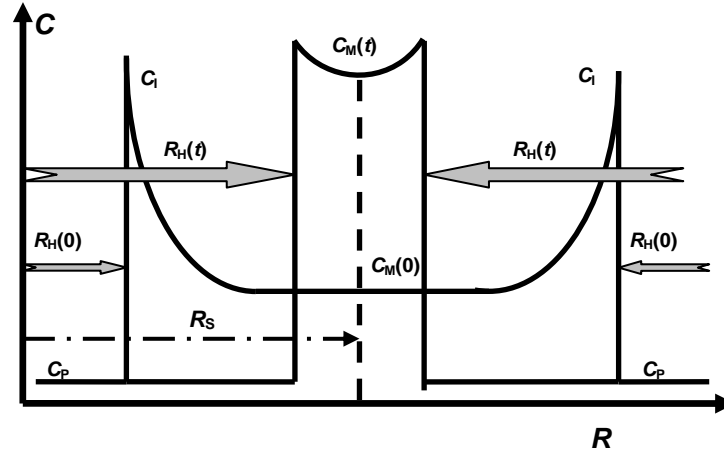


Fig. 18. The schematic representation of the "soft impingement" of growing primary nanocrystals. The symbols on the graph are described in text.

Similarly to Ham a steady state flux balance equation

$$\frac{dr(t)}{dt} = \left[\frac{C_I - C_M(t)}{C_I - C_P} \right] \frac{D}{r(t)}, \quad (1)$$

and the conservation of solute law:

$$\frac{4\pi}{3} (C_P - C_I) [r^3(t) - r^3(0)] = \frac{4\pi}{3} r_s^3 [C_M(0) - C_M(t)], \quad (2)$$

have been considered. (Here: C_P is the solute concentration in the particle, C_I is the matrix concentration at the particle interface, $C_M(0)$ and $C_M(t)$ are the matrix initial and average concentration as a function of time, respectively; $r(0)$ and $r(t)$ are the initial and time-dependent particle radii, respectively, $2r_s$ is the interparticle spacing, D is the volume diffusion coefficient (Fig. 18)).

Assuming that the effect of diffusion field impingement becomes dominating at the final stage of crystal growth where $C_M(t) \rightarrow C_I$ (Fig. 18) the solution of the system of Eqs. (1) and (2) yields the approximate expression of the crystal radius change on time at the final stage of primary crystallization as [39]

$$r(t) = \left\{ r^2(0) + (2/3) r_s^2 \lambda_H^2 [1 - \exp(-3\lambda_H Dt / r_s^2)] \right\}^{1/2}, \quad (3)$$

where $\lambda_H = [(C_M(0) - C_I) / (C_P - C_I)]^{1/3}$.

It should be noted that for the case of free growth of nanocrystals, i.e., $r_s \rightarrow \infty$ Eq. (3) transforms into the well-known Zener equation of parabolic growth [40]

$$r_z(t) = \lambda_z \sqrt{Dt} \quad (4)$$

(with $\lambda_z = [2(C_I - C_M(0)) / (C_I - C_P)]^{1/2}$) thus, lending support to the correctness of the analysis.

In view, that even for the case of nanocrystallization the final size of nanocrystals is higher than the critical nucleus radius, R_0 , Eq. (3) may be further simplified to

$$r_H(t) \approx \sqrt{2/3} \lambda_H r_s [1 - \exp(-3\lambda_H Dt / r_s^2)]^{1/2}. \quad (5)$$

As can be seen from Fig. 18 the majority of the parameters of Eq. (5) with the exception of D and C_I can be determined from the X-ray diffraction data analysis of the isothermally annealed samples. Taking into

account, that $r_H(t)$ weakly depends on C_1 and taking the matrix concentration at the particle interface equal 0.25 which corresponds the most typical chemical composition of intermetallic compounds ($Al_3(TM,RE)$) a comparison between the experimentally measured and calculated $L(t) = 2r_H(t)$ dependencies provides an opportunity for experimental verification of Eq. (5) as well for estimation of the values of D .

For these purposes the samples of amorphous $Al_{90}Y_{10}$ and $Al_{86}Ni_6Co_2Gd_6$ ribbons have been isothermally annealed for different times at several temperatures and the average sizes of Al-nanocrystals, L , as well as $r_S (= [6/(\pi N)]^{1/3})$ have been evaluated from the X-ray diffraction patterns. Such obtained $L(t)$ data have then been fitted by Eq. (5) varying the values of D . The results of this analysis are shown in Figures 19 and 20. It can be seen that the calculated $2r_H(t)$ curves are well approximate the shape of those obtained from the experimental data and within the experimental uncertainty are in good accordance indicating the validity of the proposed model of the growth.

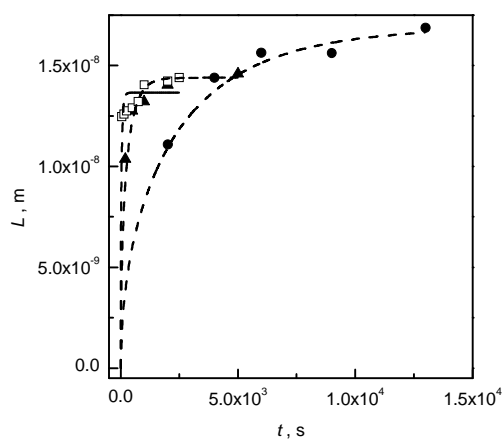


Fig. 19. Changes of the average grain size of Al-nanocrystals in amorphous $Al_{90}Y_{10}$ alloy at isothermal annealing at 447 (●), 458 (▲) and 487 K (□). The dashed curves were fitted by Eq. (5).

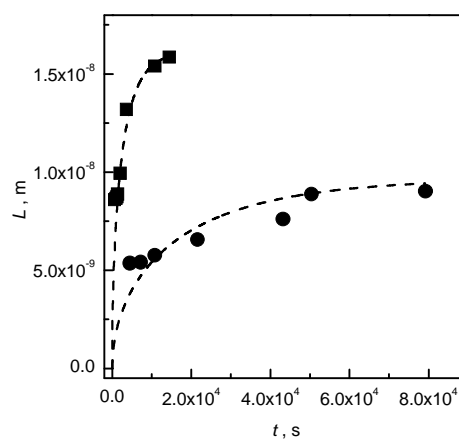


Fig. 20. Changes of the average grain size of Al-nanocrystals in amorphous $Al_{86}Ni_6Co_2Gd_6$ alloy at isothermal annealing at 443 (●) and 473 K (■). The dashed curves were fitted by Eq. (5).

The values of D for amorphous $Al_{90}Y_{10}$ and $Al_{86}Ni_6Co_2Gd_6$ alloys extracted from this analysis have been approximated by Arrhenius temperature dependencies as shown in Fig. 21. The values of the pre-exponential factor and activation energy estimated from these linearized data yield the following relationships [m^2/s]: $D(T) = 573.6 \times \exp(-22965/T)$ and $D(T) = 2.92 \times 10^{-4} \exp(-17590/T)$ for $Al_{90}Y_{10}$ and $Al_{86}Ni_6Co_2Gd_6$ alloys, respectively. A comparison between these values of D and the coefficient of self-diffusion of fcc Al [41] shows (Fig. 21) that the effective coefficient of diffusion which governs the growth of Al nanocrystals in amorphous $Al_{86}Ni_6Co_2Gd_6$ alloy is lower while that in $Al_{90}Y_{10}$ alloy is appreciably higher than D_{Al} . The latter result is somewhat unexpected in view of the features of the growth mechanism involving the rejection of the larger atoms of Y from Al nanocrystals. However, on the one hand, it is known that the mobility of atoms in amorphous phases is in general higher than that in crystals [42] and a physical meaning of the effective diffusion coefficients used in the proposed model is not well understood on the other hand. Besides, as it has been shown [43] the tails at the kinetic nanocrystallization curves may be caused not only by soft impingement considered within the presented model, but may be result of branching of Al nanocrystals. So, further investigations are required to provide more convincing evidence for both the validity of the model proposed and the refinement of the parameters.

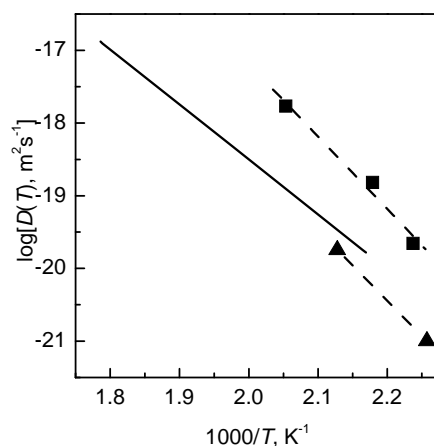


Fig. 21. Comparison of the temperature dependencies of the effective diffusion coefficients which govern Al-nanocrystals growth in amorphous Al₉₀Y₁₀ (■) and Al₈₆Ni₆Co₂Gd₆ (▲) extracted from the data shown in Figs. 19, 20 with the self diffusion coefficient of fcc Al [41] (solid lines). The dashed lines are linear approximation of the estimated data.

Another noteworthy feature of the analysis performed is that the activation energy of the effective diffusion coefficient in amorphous Al₉₀Y₁₀ alloy (22965 K) coincides with that determined above from the Kissinger analysis (22600 K), Table 1, whereas for Al₈₆Ni₆Co₂Gd₆ alloy the activation energy of the diffusivity (17590 K) is only about one-half of that of nanocrystallization (34300 K). This result suggests that the diffusion-limited growth of Al nanocrystals plays the key role in the first crystallization stage of amorphous Al₉₀Y₁₀ alloy while nanocrystallization of Al₈₆Ni₆Co₂Gd₆ is the more complicated process which the most probably involves nucleation. Note, that this assumption agrees with the results of the nanocrystallization kinetic analysis presented in Section 2.2.

In order to clarify the mechanisms of nanocrystallization the theoretical models of kinetics are required and this work is now underway.

3. Conclusions

1. Crystallization of a series of 12 binary, ternary, quaternary and quinary amorphous Al₉₀₋₈₆(Ni,Co,Fe)₆₋₈(Y,Gd,Tb)₆₋₁₀ alloys begins at temperatures 440–584 K by formation of the nanocomposite structures (nanocrystals embedded in the residual amorphous matrix) and occurs in 2 or 3 well-defined stages.
2. The three different nanocrystallization paths at the first crystallization stage have been established including: (1) diffusion limited growth of the quenched-in Al nuclei, (2) nucleation and subsequent diffusion limited growth of Al nanocrystals and (3) nucleation and simultaneous growth of nanoscale crystals of Al and intermetallic compounds.
3. Partial substitution of Gd for Y and (Y + Tb) have no appreciable influence on both thermal stability of amorphous phases and crystallization mechanism while partial replacement of Ni with Co and Fe results in enhancement of the onset crystallization temperature and finally (for proportion 1/3) in change of the nanocrystallization mechanism from primary governed by nucleation and subsequent diffusion limited growth of Al nanocrystals to eutectic-like involving transient nucleation.
4. The activation energies of the first crystallization stage are in the range from 17000 to 65800 K and its values do not correlate with thermal stability of the amorphous phases.
5. The common feature of all kinetic nanocrystallization curves is the tails at high temperature sides of the peaks of the rates of crystallization indicating the retardation of the process due to intrinsic reasons.
6. Formation of nanophase composites having the crystallized volume fractions, the average sizes of Al nanocrystals and the densities in the ranges (0.22–0.59), (14.8–21.0) nm and (1.1–4.3)×10²³ m⁻³, respectively, results in essential increasing of the microhardness (by 740–1740 MPa) in comparison with that of amorphous phases.

7. The H_{μ} values of the nanophase composite structures formed in $\text{Al}_{87}\text{Ni}_8\text{Y}_5$, $\text{Al}_{87}\text{Ni}_8\text{Gd}_5$ and $\text{Al}_{86}\text{Ni}_2\text{Co}_6\text{Gd}_6$ alloys (5200, 5180 and 5100 MPa, respectively) are close to the highest values reported in the literature.
8. The structural parameters of nanophase composites at the final stage of first crystallization step involving nucleation are dependent on the regime of heat treatment, in particular, isothermal annealing results in enhanced both the volume fraction and density of Al nanocrystals with smaller sizes compared with those obtained at constant rate heating.
9. The second stage of crystallization of amorphous $\text{Al}_{90}\text{Y}_{10}$ alloy occurs by steady state nucleation and diffusion-limited growth of Al_3Y intermetallic crystals and by coarsening of the Al nanocrystals while mechanism of this stage in amorphous $\text{Al}_{86}\text{Ni}_6\text{Co}_2\text{Gd}_6$ alloy which results in enlargement of Al nanocrystals sized is debatable.
10. It is established that the changes of the Al nanocrystals sizes in amorphous $\text{Al}_{90}\text{Y}_{10}$ and $\text{Al}_{86}\text{Ni}_6\text{Co}_2\text{Gd}_6$ alloys during isothermal annealing may be satisfactory described within the proposed analytical model assuming retardation of the diffusion-limited growth due to impingement of the diffusion fields.
11. The extracted from the experimental data effective diffusion coefficients governing the growth of nanocrystals in amorphous $\text{Al}_{86}\text{Ni}_6\text{Co}_2\text{Gd}_6$ alloy are somewhat lower while those in $\text{Al}_{90}\text{Y}_{10}$ alloy are higher than the self diffusion coefficient of crystalline Al.
12. All studies have been carried out according with the working plan.

4. References

1. He Y., Poon S.J. and Shiflet G.J. Synthesis and properties of metallic glasses that contain aluminum // Science – 1988. - Vol. 241. - pp. 1640-1642.
2. Inoue A. Amorphous, nanoquasicrystalline and nanocrystalline alloys in Al-based systems // Progr. Mater. Sci. – 1998. – **43**. – pp. 365–520.
3. Chen H., He Y., Shiflet G.J., Poon S.J. Mechanical properties of partially crystallized aluminium based metallic glasses // Scr. Met. Mater. – 1991. – v. 25, No 6. – pp. 1421–1424.
4. Choi G.S., Kim Y.H., Cho H.K., Inoue A., Masumoto T. Ultrahigh tensile strength of amorphous Al-Ni-(Nd,Gd)-Fe alloys containing nanocrystalline Al particles // Scr. Metall. et Mater. – 1995. – V. 33, No 8. – pp. 1301-1306.
5. Sanders W.S., Warner J.S., Miracle D.B. Stability of Al-rich glasses in the Al-La-Ni system // Intermetallics – 2006. – vol. 14. – pp. 348-351.
6. Senkov O.N., Miracle D.B., Scott J.M., Senkova S.V. Equal channel angular extrusion compaction of semi-amorphous $\text{Al}_{85}\text{Ni}_{10}\text{Y}_{2.5}\text{La}_{2.5}$ alloy powder // J. Alloys and Compounds – 2004. – Vol. 365. – pp. 126-133.
7. Shpak A.P., Varyukhin V.N., Tkatch V.I., Maslov V.V., Beygelzimer Y.Y., Synkov S.G., Nosenko V.K., Rassolov S.G. Nanostructured $\text{Al}_{86}\text{Gd}_6\text{Ni}_6\text{Co}_2$ bulk alloy produced by twist extrusion of amorphous melt-spun ribbons // Mater. Sci. Eng. A – 2006. – v. 425. – pp. 172-177.
8. Wang J.O., Zhang H.W., Gu X.J., Lu K., Sommer F., Mittemeijer E.J. Kinetics of primary nanocrystallization in Al-rich metallic glass with quenched-in nuclei // Mater. Sci. Eng. A – 2004. – Vols. 375-377. – pp. 980-984.
9. Battezzati L., Rizzi P., Ronto V. The difference in devitrification paths in $\text{Al}_{87}\text{Ni}_7\text{Sm}_6$ and $\text{Al}_{87}\text{Ni}_7\text{La}_6$ amorphous alloys // Mater. Sci. Eng. A – 2004. – Vols. 375-377. – pp. 927-931.
10. Yavari A. R., Negri D. Effect of concentration gradients on nanostructure development during primary crystallization of soft-magnetic iron-based amorphous alloys and its modeling // NanoStruct. Mater. – 1997. – **8**, No 8. - pp. 969–986.
11. Kusy M., Riello P., Battezzati L. A comparative study of primary Al precipitation in amorphous $\text{Al}_{87}\text{Ni}_7\text{La}_5\text{Zr}$ by means of WAXS, SAXS, TEM and DSC techniques // Acta Mater. – 2004. – Vol. 52. – pp. 5031-5041.
12. Wesseling P., Ko B.C., Lewandowski J.J. Quantitative evaluation of α -Al nano-particles in amorphous $\text{Al}_{87}\text{Ni}_7\text{Gd}_6$ – comparison of XRD, DSC, and TEM // Scr. Mater.- 2003.- V. 48.- pp. 1537-1541.
13. Gloriant T., Gich M., Surinach S., Baro M.D., Greer A.L. Evaluation of the volume fraction crystallized during devitrification of Al-based amorphous alloys // Mater. Sci Forum – 2000.- V. 343-436. – pp. 365-370.

14. Blazquez J.S., Franco V., Conde C.F., Conde A. Microstructure and magnetic properties of $\text{Fe}_{78-x}\text{Co}_x\text{Nb}_6\text{B}_{15}\text{Cu}_1$ ($x = 18, 39, 60$) alloys // *JMMM*. – 2003. – V. 254-255. – pp. 460-462.
15. Huang Z.H., Li J.F., Rao Q.L., Zhou Y.H. Effects of replacing Ni by Co on the crystallization behaviors of Al-Ni-La amorphous alloys // *Intermetallics* – 2008. – vol. 16. – pp. 727-731.
16. Wang S.H., Bian X.F. Effect of Si and Co on the crystallization of Al-Ni-RE amorphous alloys // *J. Alloys and Comp.* – 2008. – vol. 453. – pp. 127–130.
17. Mika T., Karolus M., Haneczok G., Bednarska L., Lagiewka E., Kotur B. Influence of Gd and Fe on crystallization of $\text{Al}_{87}\text{Y}_5\text{Ni}_8$ amorphous alloy // *J. Non-Cryst. Sol.* – 2008. – vol. 354. – pp. 3099–3106.
18. Yang H.W., Tjong S.C., Wang J.Q. Influence of Fe addition on glassy stability of an $\text{Al}_{85}\text{Ni}_5\text{Y}_8\text{Co}_2$ metallic glass with a large supercooled liquid region // *Mater. Sci. Eng. A* – 2005. – vol. 406. – pp. 160-165.
19. Kissinger H.E. Variation of peak temperature with heating rate // *J. Res. Nat. Bur. Stand.*- 1956.- **57**, No 4.- pp. 217–220.
20. Massalski T.B. Binary alloy phase diagrams, American Society for Metals, Metals Park, OH, 1986.
21. Antonowicz J., Jaskiewicz P., Nowinski L., Pekala K. Analysis of nanocrystallization process of amorphous $\text{Al}_{90}\text{Y}_{10}$ alloy // *J. Non-Cryst. Solids* – 2003. – V. 329. – pp. 77-81.
22. Gao M.C., Shiflet G.J. Devitrification phase transformations in amorphous $\text{Al}_{85}\text{Ni}_7\text{Gd}_8$ alloy // *Intermetallics*. – 2002. – Vol. 10. – pp. 1131-1139.
23. Mudry S., Bernadska L., Kulyk Y., Kotur B., Kovbuz M., Hertsyk O. Temperature changes of structure in $\text{Al}_{87}\text{Ni}_8\text{Y}_5$ amorphous alloy // *Arch. Mater. Sci.* – 2004. – Vol. 25, No 4. – pp. 373-278.
24. Zhuang Y.X., Jiang J.Z., Lin Z.G., Mezouar M., Crichton W., Inoue A. Evidence of eutectic crystallization and transient nucleation in $\text{Al}_{89}\text{La}_6\text{Ni}_5$ amorphous alloy // *Appl. Phys. Lett.* – 2001. – Vol. 79, No 6. – pp. 743-745.
25. Allen D.R., Foley J.C., Perepezko J.H. Nanocrystal development during primary crystallization of amorphous alloys // *Acta Mater.* – 1998. – **46**, No 2. – pp. 431-440.
26. Zhong Z. C., Jiang X. Y., Greer A. L. Microstructure and hardening of Al-based nanophase composites // *Mater. Sci. Eng. A* – 1997. – Vols. 226-228 – pp. 531-535.
27. Mechanisms for nanocrystals formation in metallic alloys // K.F. Kelton, T.K. Croat, A.K. Gangopadhyay, L.-Q. Xing, A.L. Greer, M. Weyland, X. Li, K. Rajan / *J. Non-Cryst. Sol.* – 2003. – v. 317. – pp. 71-77.
28. Clavaguera-Mora M.T., Clavaguera N., Crespo D., Pradell T. Crystallisation kinetics and microstructure development in metallic systems // *Progr. Mater. Sci.* – 2002. – Vol. 47. – pp. 559-619.
29. U. Köster, and U. Herold, in “Glassy Metals I, Topics in Applied Physics” (H. J. Günterodt and H. Beck, eds), Vol. 46, p. 225. Springer-Verlag, 1981, p. 230.
30. Christian J.W. *The Theory of Transformations in Metals and Alloys*. – Oxford: Pergamon, 1965. – 845 p.
31. Munoz-Morris M.A., Surinach S., Baro M.D., Morris D.G. Influence of annealing treatments on crystallization and mechanical properties of a Al-4Ni-6Ce glass // *Mater. Sci. Eng. A* – 2004. – Vols 375-377. – pp. 965-968.
32. Kim T.-S., Hong S.-J., Lee B.-T. Hardness behavior of the partially crystallized amorphous $\text{Al}_{86}\text{Ni}_9\text{Mm}_5$ alloys // *Mater. Sci. Eng. A* – 2003. – Vol. 363. – pp. 81–85.
33. Rizzi P., Doglione R., Battezzati L. Mechanical properties of Al-based amorphous/nanocrystalline alloys // *Mater. Sci. Eng. A* – 2004. – Vols 375-377. – pp. 969-974.
34. Antonowicz J. Time resolved X-ray diffraction study of nanocrystallization in Al-based metallic glasses // *J. Non-Cryst. Solids* – 2005. – Vol. 351. – pp. 2383-2387.
35. Sahoo K.L., Wollgarten M., Haug J., Banhart J. Effect of La on the crystallisation behaviour of amorphous $\text{Al}_{94-x}\text{Ni}_6\text{La}_x$ ($x = 4-7$) alloys // *Acta Mater.* – 2005. – Vol. 53. – pp. 3861-3870.
36. Sahoo K.L., Panda A.K., Das S., Rao V. Crystallization study of amorphous $\text{Al}_{87}\text{Ni}_7\text{Mm}_5\text{Fe}_{0.5}$ alloy by electrical resistivity measurement // *Mater. Lett.* – 2004. – vol. 58. – pp. 316–320.
37. Hono K., Zhang Y., Tsai A.P., Inoue A., Sakurai T. Solute partitioning in partially crystallized Al-Ni-Ce(-Cu) metallic glasses // *Scr. Metall. Mater.* – 1995. – Vol. 32, No 2. – pp. 191-196.
38. Ham F.S. Theory of diffusion-limited precipitation // *J. Phys. Chem. Solids* – 1958. – **6**. – pp. 335-351.
39. Tkatch V.I., Rassolov S.G., Moiseeva T.N., Popov V.V. Analytical description of isothermal primary crystallization of glasses: $\text{Fe}_{85}\text{B}_{15}$ // *J. Non-Cryst. Solids* – 2005. – Vol. 351. – pp. 1658-1664.

40. Zener C. Theory of growth of spherical precipitates from solid solution // J. Appl. Phys. – 1949. – Vol. 20, No 10. – pp. 950-953.
41. Properties of elements (edited by G.V. Samsonov), Moscow: Metallurgy, 1976 (in Russian).
42. Faupel F., Frank W., Macht M.-P., Mehrer H., Naundorf V., Ratzke K., Shrober H.R., Sharma S.K., Teichler H. Diffusion in metallic glasses and supercooled melts // Rev. Mod. Phys. – 2003. – v. 75. – pp. 237-280.
43. Nitsche H., Sommer F., Mittemeijer E.J. The Al nano-crystallization process in amorphous $\text{Al}_{85}\text{Ni}_8\text{Y}_5\text{Co}_2$ // J. Non-Cryst. Solids – 2005. – Vol. 351. – pp. 3760-3771.

7. List of Symbols, Abbreviations, and Acronyms

1	T_{ons}	- temperature of transformation onset;
2	R	- electrical resistivity
3	RE	- rare earth metals;
4	TM	- transition metals;
5	H_{H}	- microhardness;
6	L	- size (diameter) of nanocrystals;
7	XRD	- X-ray diffraction;
8	x	- concentration in atomic percents;
9	X	- volume fraction of crystalline phase;
10	λ	- X-ray wave length;
11	θ	- angle positions of the maxima;
12	N	- volume density of nanocrystals;
13	D	- coefficient of diffusion;
14	r	- radius of nanocrystal;
15	n	- Avrami exponent;
16	T_{X}	- temperature of maximum rate of transformation;
17	q	- rate of heating;
18	Q	- activation energy;